ChemSusChem

Ultrathin mesoporous RuCo2O4 nanoflakes: A novel advanced electrode for high performance asymmetric supercapacitors

--Manuscript Draft--

Manuscript Number:	
Article Type:	Full Paper
Corresponding Author:	Deepak Dubal, Ph.D. Spain Barcelona, SPAIN
Corresponding Author E-Mail:	dubaldeepak2@gmail.com
Order of Authors (with Contributor Roles):	Deepak Dubal, Ph.D.
	Nilesh Chodankar
	Rudolf Holze
Keywords:	Ruthenium cobalt oxide, Ultrathin Nanoflakes, Supercapacitor
Manuscript Classifications:	Batteries; Electrode materials; Energy storage; Supercapacitors
Suggested Reviewers:	Yuping Wu wuyp@fudan.edu.cn
	Keryn Lian keryn.lian@utoronto.ca
	Maria João Pedroso Carmezim maria.carmezim@estsetubal.ips.pt
	Rongming Wang rmwang@ustb.edu.cn
Opposed Reviewers:	
Abstract:	Herein, a novel ruthenium cobalt oxide (RuCo2O4) as an advanced electrode material has been successfully prepared with unique marigold-like nanostructure by a simple electrodeposition (potentiodyanamic mode) method. The RuCo2O4 marigolds consist of numerous clusters of ultrathin mesoporous nanoflakes, leaving a large interspace between them to provide numerous electrochemically active sites. Strikingly, this unique marigold-like nanostructure provides excellent electrochemical performance in terms of high energy storing capacity (1469 F/g at 6 A/g) with excellent rate proficiency and long-lasting operating cycling stability (around 91.3 % capacitance retention after 3000 cycles), confirming all mesoporous nanoflakes participate in the ultrafast electrochemical reactions. Later, asymmetric capacitor was assembled using RuCo2O4 (positive electrode) and activated carbon (AC) (negative electrode) with aqueous KOH electrolyte. The asymmetric design allows upgraded potential range of 1.4 V, which further provides good energy density of 32.6 Wh/kg (1.1 mWh/cm3). More importantly, the cell delivers the energy density of 12.4 Wh/kg even at maximum power density of 3.2 kW/kg, which is noticeably more than the carbon based symmetric systems.
Author Comments:	To, The Editor, ChemSusChem Dear Editor, This submission implies online submission of our recent novel investigation entitled "Ultrathin mesoporous RuCo2O4 nanoflakes: A novel advanced electrode for high performance asymmetric supercapacitors" Deepak P. Dubal,a* Nilesh R. Chodankar,b Rudolf Holze,c for publication in ChemSusChem After the successful implementation of NiCo2O4, as an excellent material for battery and supercapacitors, the search of other mixed transition metal oxide is obvious.

	Recently, many investigations were studied different ternary metal oxides such as $MnCo_2O_4$, $CoFe_2O_4$, $NiMn_2O_4$ etc. and many more are under investigation. In this context, we are first time introducing a novel ternary metal oxide as ruthenium cobalt oxide ($RuCo_2O_4$) for supercapacitor application. This material has a unique combination of well-known pseudo-capacitive RuO_2 and intrinsically battery material Co_3O_4, leading to the synergetic charge storing mechanisms. In this first attempt, we have designed marigold-like ruthenium cobalt oxide ($RuCo_2O_4$) ultrathin mesoporous nanoflakes on stainless steel substrate with potentiodynamic (cyclic voltammetry) mode of a simple one-step electrodeposition method. These $RuCo_2O_4$ marigolds composed of millions of ultrathin mesoporous nanoflakes exhibits remarkable capacitive performances. Several physico-chemical characterization techniques are used to justify clear evidences of formation of this materials and its potential as promising electrode material for supercapacitors. In the next step, we have designed asymmetric capacitor with $RuCo_2O_4$ as positive electrode and activated carbon as negative electrode. The AC//$RuCo_2O_4$ cell delivers a high energy density of 32 Wh/kg which is comparable to the values reported for $NiCo_2O_4$ based materials and considerably higher than carbon based materials. Further improvement in the electrochemical properties of $RuCo_2O_4$ electrodes can be achieved by synthesizing different nanostructures. This investigation introduces new material which can have other possible applications such as battery, magnetic properties etc. I really hope you will agree that this excellent report could be a promising article for many interesting reports to come. I look forward to your news Best Regards Dr. Deepak P. Dubal, Ph. D. Marie-Curie Fellow (BP-DGR), (AvH, Germany) Catalan Institute of Nanoscience and Nanotechnology, CIN2, ICN2 (CSIC-ICN) Campus UAB, E-08193 Bellaterra (Barcelona), Spain
Section/Category:	
Additional Information:	
Question	**Response**
Dedication	No dedication
Submitted solely to this journal?	Yes
Has there been a previous version?	No
Do you or any of your co-authors have a conflict of interest to declare?	No. The authors declare no conflict of interest.

Ultrathin mesoporous $RuCo_2O_4$ nanoflakes: A novel advanced electrode for high performance asymmetric supercapacitors

Deepak P. Dubal,[a] Nilesh R. Chodankar,[b] Rudolf Holze,[c]*

[a]Catalan Institute of Nanoscience and Nanotechnology (ICN2), The Barcelona Institute of Science and Technology (CSIC-BIST), Campus UAB, Bellaterra, 08193 Barcelona, Spain

[b]School of Applied Chemical Engineering, Chonnam National University, Gwangju 500-757, South Korea

[b]Technische Universität Chemnitz, Institut für Chemie, AG Elektrochemie, D-09107 Chemnitz, Germany

CORRESPONDING AUTHOR FOOTNOTE

Dr. Deepak Dubal,

Tel.: +349373609/+34937373608 Fax: + 34936917640

E-mail: dubaldeepak2@gmail.com (D. Dubal),

Abstract

Herein, a novel ruthenium cobalt oxide ($RuCo_2O_4$) as an advanced electrode material has been successfully prepared with unique marigold-like nanostructure by a simple electrodeposition (potentiodyanamic mode) method. The $RuCo_2O_4$ marigolds consist of numerous clusters of ultrathin mesoporous nanoflakes, leaving a large interspace between them to provide numerous electrochemically active sites. Strikingly, this unique marigold-like nanostructure provides excellent electrochemical performance in terms of high energy storing capacity (1469 F/g at 6 A/g) with excellent rate proficiency and long-lasting operating cycling stability (around 91.3 % capacitance retention after 3000 cycles), confirming all mesoporous nanoflakes participate in the ultrafast electrochemical reactions. Later, asymmetric capacitor was assembled using $RuCo_2O_4$ (positive electrode) and activated carbon (AC) (negative electrode) with aqueous KOH electrolyte. The asymmetric design allows upgraded potential range of 1.4 V, which further provides good energy density of 32.6 Wh/kg (1.1 mWh/cm^3). More importantly, the cell delivers the energy density of 12.4 Wh/kg even at maximum power density of 3.2 kW/kg, which is noticeably more than the carbon based symmetric systems.

Introduction

Presently, a ternary transition metal oxide, which is a combination of two different metals, are evolving as encouraging materials for advanced energy storage systems including the supercapacitors and Li-ion batteries [1-4]. The pairing of two different metals can enrich the redox chemistry of the material which is extremely favorable for electrochemical systems. Moreover, the unique chemical combination and joint effects of different metal species delivers outstanding electrochemical performances than the eminent supercapacitive electrodes materials like carbon and metal oxides [5-8]. Moreover, because of the several possible cation combinations and the easy tuning of stoichiometric/non-stoichiometric ratios, the capacitive properties of these ternary metal oxides can be certainly manipulated. For example, many compositions such as $NiCo_2O_4$, $CoFe_2O_4$ and $NiMn_2O_4$ have already been studied for supercapacitors [9-12]. Thus, $NiCo_2O_4$ is the one which is comprehensively studied however there are very few reports are available for other possible cation combinations.

The key factor, on which the electrochemical properties of supercapacitors rely is the characteristics of the electrode materials such as crystal structure, surface morphologies and surface properties (surface area, porosity etc.) [13-19]. In particular, designing hierarchical architectures such as nanorods, nanoflakes, nanosheets etc. are of special interest and attracted a great attention of many materials scientists due to their outstanding properties. It is expected that, these hierarchical nanostructures offer many advantages such as enhanced stability, unique pore size distribution and low diffusion paths, which are greatly influential factors on electrochemical performance [20-22]. However, synthesis of ternary metal oxide with unique nanostructure and appropriate cation composition is quiet a challenging task. Therefore, it is anticipated that to prepare the innovative ternary metal oxide through the simple method having unique composition and hierarchical architecture, which must offers outstanding electrochemical performances to enhance the energy storing capacity of supercapacitor.

Consequently, to overcome the above discussed issues, we introduce a very simple but capable electrochemical approach to synthesize novel marigold-like ruthenium cobalt oxide ($RuCo_2O_4$) ultrathin mesoporous nanoflakes on stainless steel substrate with remarkable capacitive performance. These $RuCo_2O_4$ marigolds composed of millions of ultrathin mesoporous nanoflakes are prepared with potentiodynamic (cyclic voltammetry) mode of a simple one-step electrodeposition with subsequent annealing. The relations between preparative parameters and morphological and consequently electrochemical properties of RCO thin films are systematically investigated. To provide practical realization, further asymmetric capacitor was assembled using $RuCo_2O_4$ (positive electrode) and activated carbon (AC) (negative electrode) in 2 M KOH electrolyte. The electrochemical properties of $RuCo_2O_4$//AC cells were investigated in details.

Experimental details

Thin films of $RuCo_2O_4$ were prepared by single step potentiodynamic mode of electrodeposition on to the stainless steel (SS) substrate. Before deposition, we polished the SS substrate with sand paper and then successively cleaned with acetone and deionized water. The solution containing 10 mM $RuCl_3.xH_2O$ and 20 mM $CoCl_2{\cdot}6H_2O$ in deionized water (pH~4) was used for the potentiodynamic deposition of $RuCo_2O_4$ thin films. A conventional electrochemical set-up comprising three electrode system including SS as working, graphite as counter and Ag/AgCl reference electrodes. The potentiodynamic mode was employed to deposit the $RuCo_2O_4$ thin films in potential limit of -1.0 to 0.0 V (vs Ag/AgCl) at different scanning rates of 25, 50 and 100 mV/s. The samples prepared at scan rates of 25, 50 and 100 mV/s are titled as RCO25, RCO50 and RCO100, respectively.

Results and Discussion

The growth mechanism of $RuCo_2O_4$ thin films is explained by considering the deposition CV curves, which is presented in supporting information (see supporting information S.I. S1). Figure S1 (a) shows the first CV cycle in $RuCo_2O_4$ precursor solution at 25 mV/s scan rate

between potentials of -1.0 to 0 V (vs, Ag/AgCl). In initial region of the CV curves, the slightly increment in current is observed up to -0.34 V (vs Ag/AgCl), after that it stabilize till the potential reach to -0.69 V (vs Ag/AgCl) which showing one reduction peak at -0.56 V (vs Ag/AgCl). That means the deposition of metals (Ru-Co) initiates at around -0.35 V (vs Ag/AgCl). In this potential region, the monolayers formation initiated accordingly with the characteristics of the underpotential conditions [23-26]. The possible reaction for the formation of the $RuCo_2O_4$ is given below (eq. 2).

$$M^{2+}{}_{(aq)} + 2OH^{-}{}_{(aq)} \Rightarrow M(OH)_{2(s)} \text{ where M = Ru or Co} \qquad (1)$$

Afterwards, from -0.7 to -1 V the current increased rapidly which suggest the nucleation process at the stainless steel substrate. In the overpotential region (at around -1.0 V,), 3D nucleation and growth of Ru-Co is occurred. At this potential, random and massive deposition of Ru-Co is occurred on the SS electrode [27]. On the other hand, the current density was significantly higher on the reverse scan until -0.7 V. The CV curve presents metal reduction reaction, particularly the “nucleation loop” towards the negative limit and two dissolution (oxidation) peaks (II and III) are observed in the reverse scan at potentials of -0.33 V and -0.15 V (vs Ag/AgCl), respectively. The cathodic crossover around -0.71 V corresponds to the nucleation overpotential confirming the point of nucleation and growth mechanism. Interestingly, the current under the curve as well as the intensity of redox peaks increases with number of cycles suggesting the electronic conductance of $RuCo_2O_4$ films (S.I. S1 (b)). Finally, after growth completion, the films were cleaned with deionized water and air-annealed at 623 K in order to convert them into $RuCo_2O_4$.

$$M(OH)_{2(s)} \xrightarrow{623K} RuCo_2O_4 \qquad (2)$$

Further, the samples are prepared at various scanning rate (25, 50 and 100 mV/s) to investigate the effect of scan rate on the electrochemical features of $RuCo_2O_4$ thin films. The increasing scan rate gradual upsurge the current density while the redox potentials does not

change, signifying that the scan rate has no impact on the deposition potentials of Ru-Co films (see S. I. S1 (c)). Note that, to check the effect of scan rate, the deposition time must be the same, hence we have varied the deposition cycles like 40, 80 and 160 cycles for the scan rate of 25, 50 and 100 mV/s, respectively. The deposited mass of $RuCo_2O_4$ on the SS electrode (on $1cm^2$) was in the range of 0.32-0.29 mg/cm^2 for the scan rate of 25-100 mV/s. At higher scan rate (more than the 100 mV/s), non-uniform and less adherent films were obtained; this may be attributed to the dominance of nucleation over particle growth.

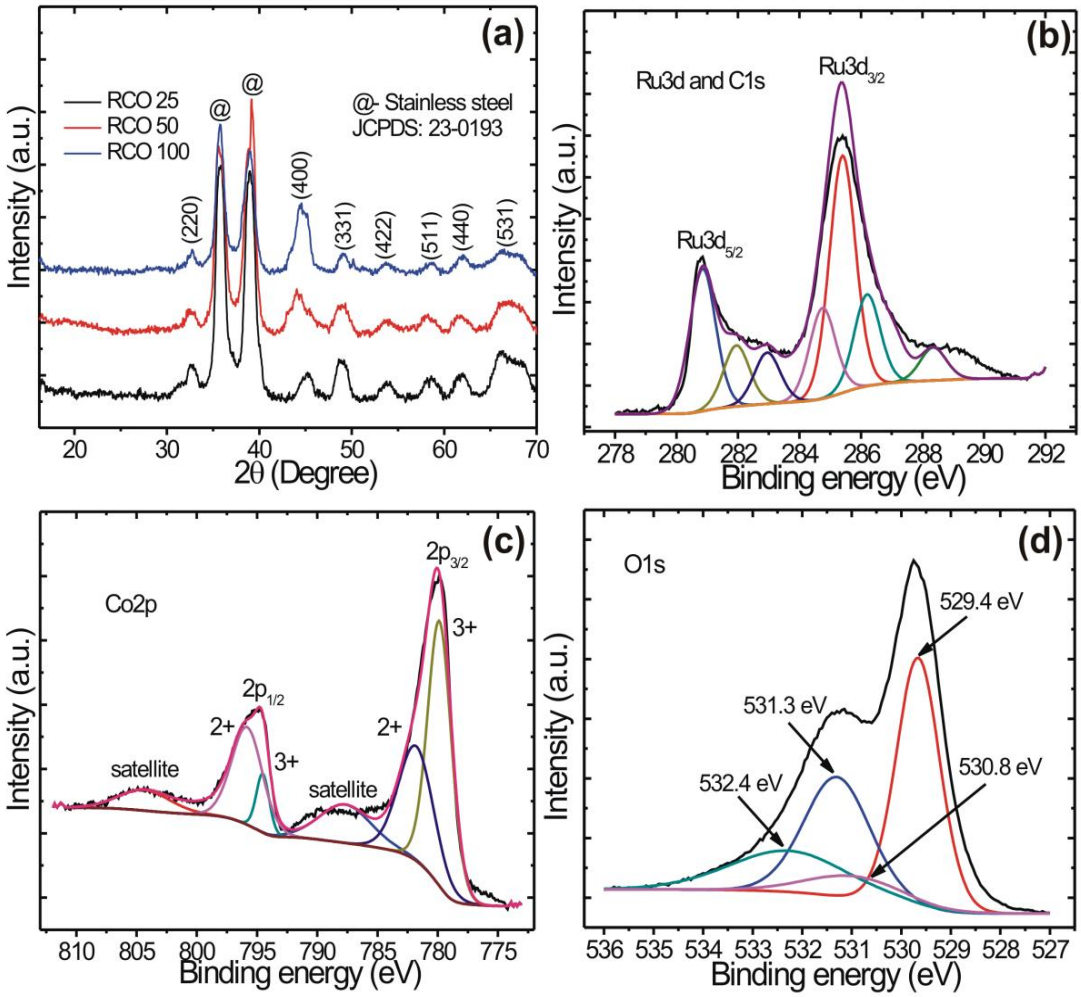

Fig. 1 (a) XRD profiles of $RuCo_2O_4$ thin film deposited on the SS electrode at various scan rates RCO25, RCO50 and RCO100. High magnified XPS spectra of (b) Ru3d and C1s (c) Co2p, (d) O 1s for $RuCo_2O_4$ mesoporous nanoflakes (RCO100).

Fig. 1 (b) display XRD patterns of $RuCo_2O_4$ films synthesized on SS substrate at different scan rates. The characteristic peaks correspond to (220), (400), (331), (422), (511), (440) and (531) diffraction planes of spinel cubic phase of $RuCo_2O_4$ [JCPDS: 23-0193]. In addition, the peaks are broad with low intensity suggesting the formation of nanocrystalline materials. Two additional peaks shown with '@' sign are attributed to the SS substrate. The lattice parameter '*a*' is calculated for the most intense peak (220) using following formula,

$$a = d_{hkl}\sqrt{h^2 + k^2 + l^2} \qquad (3)$$

where '*a*' is the lattice parameter of the unit cell, 'd_{hkl}' is the interplanar spacing and (h k l) are Miller indices for the plane (220). The calculated lattice parameter for $RuCo_2O_4$ is *a* = 8.230 Å which is in good agreement with JCPDS 23-0193 (*a* = 8.241 Å). Generally, cubic spinel-type oxides are designated with $Fd\bar{3}m$ space group and which are conveyed as (M)[M'$_2$]O_4, where M and M' are the two metal cations and which are arranged at the tetrahedral or octahedral site. In general, M is situated at the tetrahedral *A*-site, while M' is occurred at the octahedral *B*-site. In spinel structure, cobalt occurs in multiple oxidation states (+2 and +3), in which the high-spin Co^{2+} occupy at the tetrahedral *A* or octahedral *B* sites while low-spin Co^{3+} occupy only at the octahedral sites [28]. In order to further confirm the cation distribution XPS analysis of RCO100 sample was carried out (see Fig. 1 (b-d)). The full-scan survey spectrum of the material (see S.I. S2) indicates the presence of C1s, O1s, Co2p, Ru3p and Ru3d as well as the absence of any other impurities. The Ru occurs in various oxidation state like the Ru3p and Ru3d, particularly the peak fitting for Ru3d spectra is complicated and which overlap with the C1s peaks. The peak fitting of $Ru3d_{5/2}$ spectra presented in this work required at least three deconvolution curves taken from a previous report by Morgan et. al. [29]. The binding energies for deconvolution curves are 280.6 eV, 281.9 eV and 282.8 eV indicating the existence of Ru^{4+} [30-32]. Literature data are contradictory, some authors attribute the peak between 282.5-282.8 eV to Ru in the valence state (VI), RuO_3 [32, 33]. The existence of a RuO_3 phase has been

extensively debated in the literature. According to the present understanding, Ru(VI) does not form a thermodynamically stable solid RuO_3 phase, but may rather exist as a metastable phase or a defective RuO_2 phase [34]. Note that the presence of Ru(VI) cannot be excluded, but was neglected in this work due to their negligible contribution and the overlap with the C1s peaks. Moreover, full spectrum for $RuCo_2O_4$ sample (see S.I.S2) shows the peak centered at 463.7-463.8 eV for the Ru3p3/2 which further confirms the presence of Ru^{4+} in $RuCo_2O_4$ (see S.I. S2) [35]. The slight shift in the peak positions might be attributed to neighboring ion effect [35]. The peaks at 288.3, 286.2, 285.4 and 284.7eV resemble to O-C=O, C=OH, C-O-C and C-C fitted to C1s spectrum, respectively [32]. Similarly, the Co2p spectra displayed in Fig. 1 (c) exhibits two doublets for the Co^{2+} and Co^{3+}, and two shakeup peaks. The deconvulated peaks at 781.9 and 796.9 eV corresponds to Co^{2+}, while the remaining two peaks centered at 779.7 and 794.6 eV attributes to Co^{3+} [36, 37]. The O1s spectrum exhibit four major peaks centered at 532.5, 531.2 and 529.4 eV as displayed in Fig. 1 (d), associated with hydroxyl groups of surface adsorbed water, surface oxygen ions and metal-oxygen bonding, respectively [36, 37]. The small component observed at 530.8 eV suggests that the surface of $RuCo_2O_4$ thin films is hydroxylated [38]. Thus, it is clear that, the surface of $RuCo_2O_4$ contains Co^{2+}, Co^{3+}, Ru^{4+} and O^{2-}. Further characterizations are required in order to deeper understand Ru oxidation states in $RuCo_2O_4$.

To understand the growth mechanism of $RuCo_2O_4$ mesoporous nanoflakes, corresponding FESEM images obtained after deposition is carried out for different numbers of cycles from 10-40 at 25 mV/s scan rate are presented in Fig. S.I. S3. The surface nanostructure of the $RuCo_2O_4$ moderately changes with deposition cycles (see Fig. S.I. S3). As observed in the Fig. S3 (a), just after 10 deposition cycles the mesoporous nanoflakes are grown on the SS electrode along with the nanoparticles. It is further interesting to note that with increasing number of cycles from 10-40 the whole surface is totally converted from the immature nanoflakes to the mature mesoporous nanoflakes (see Fig. S3 b-d). Further increase in

deposition cycle number results in the peeling-off of $RuCo_2O_4$ mesoporous nanoflakes. In conclusion, it is clear that the potentiodynamic deposition of $RuCo_2O_4$ mesoporous nanoflakes involves two different steps: nucleation and growth. Initially, the nuclei are formed at the surface of the SS substrate through a 'self-assembly' process and then starts to grow vertically with number of cycles in order to form mesoporous nanoflakes. With the increase in number of deposition cycle, the growth of $RuCo_2O_4$ nuclei is prominent, which further aggregated and finally transformed into mesoporous nanoflakes. From the thermodynamic view point, each nanoflakes has high surface energy therefore; the vertical growth of nanoflakes is observed [39]. Thus, with the reaction time, these ultrathin mesoporous nanoflakes would self-accumulate to form an interconnected network of marigold-like $RuCo_2O_4$ architecture to minimize total surface energy.

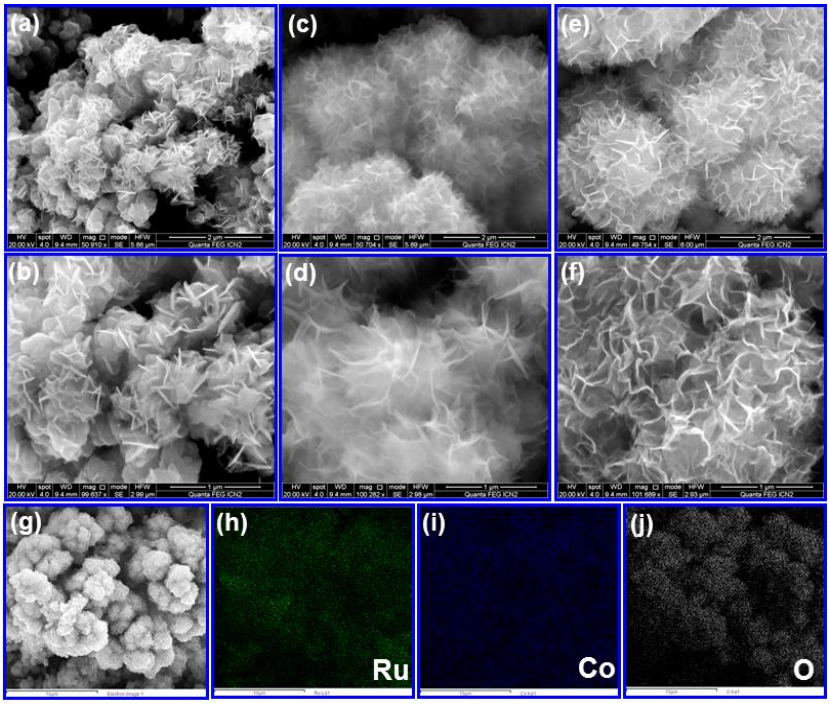

Fig. 2 FE-SEM pictures of $RuCo_2O_4$ thin films prepared at different scan rates such as (a, b) RCO25 (25 mV/s), (c, d) RCO50 (50 mV/s) and (e, f) RCO100 (100 mV/s) at two different magnifications, respectively. In addition, (g-j) SEM and corresponding EDS mapping images for RCO100 sample.

Fig. 2 presents the FESEM images of $RuCo_2O_4$ films prepared at the scan rates of 25, 50 and 100 mV/s. The increasing scan rate from 25 to 100 mV/s effectively modify the surface morphology of $RuCo_2O_4$ varies from immature nanoflakes to hierarchical open-porous and vertically aligned mesoporous nanoflakes. The film prepared at lower scan rate of 25 mV/s looks like a cluster of thin nano-petals (Fig. 2 (a, b)). Further, the enhancement in the deposition scan rate from 25 to 50 mV/s amend the surface morphology of $RuCo_2O_4$ thin film from the cluster of thin nano-petals to the relatively well-developed mesoporous nanoflakes. These nanoflakes are interconnected to each to create a spherical marigold-like architecture as seen in Fig. 2 (c). Moreover, high magnified image discovered the formation of clusters of mesoporous nanoflakes (Fig. 2 d). sample prepared at 100 mV/s scan rate shows the 3D network of highly porous marigold-like $RuCo_2O_4$ mesoporous nanoflakes (Fig. 2 e, f), On closer inspection, it is seen that $RuCo_2O_4$ marigold spheres consist of numerous clusters of ultrathin mesoporous nanoflakes, leaving a large interspace between them. Thus, the surface morphology of $RuCo_2O_4$ is surprisingly altered from the 25 to 100 mV/s scan rate which might be ascribed in following way. It is worth noting that in potentiodynamic mode the deposition of material is discontinuous which is completely different from the potentiostatic or galvanostatic modes where constant voltage or current are applied. Thus, the potentiodynamic mode exhibits deposition/dissolution of material (Ru-Co in present case) at regular interval of time. At slow scan rate (25 mV/s), the deposition and dissolution time is long which allows for more nucleation and growth of the material, resulting in relatively thick nano-petals. On the contrary, at high scan rates, the electrolyte components have very short time to deposit on the current collector, which affect the nucleation and growth rate to form the vertically aligned nanomaterial. Thus, at the lower scan rate electrolyte components have sufficient time to deposit on the current collector to form the dense and thick nano-petals like surface morphology, while at 100 mV/s scan rate, the residence time is less, leading to the formation of hierarchical marigold-like mesoporous nanoflakes. Furthermore, SEM-EDS mapping is shown in Fig. 2 (g-j) for $RuCo_2O_4$ thin film prepared at 100

mV/s scan rate. The uniform distribution of Ru, Co and O is clearly confirmed through the surface. Moreover, 13.7 %, 29.2 % and 57.1 % of Ru, Co and O are found which demonstrates the formation of the $RuCo_2O_4$ material (see S. I. S2 (b)). Some additional peaks are observed which correspond to the stainless steel substrate.

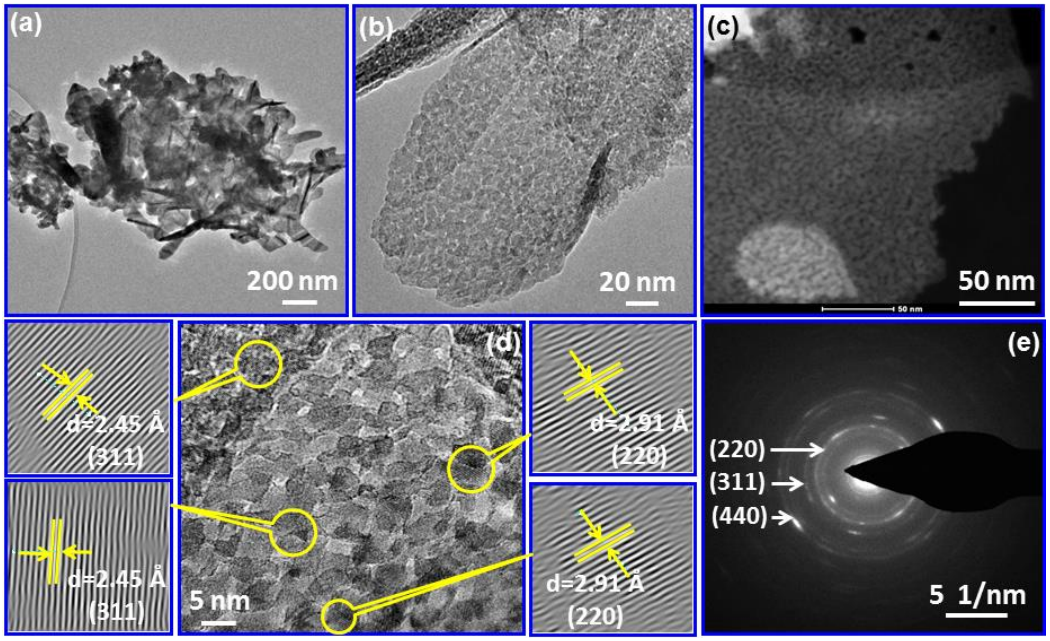

Fig. 3 TEM and HRTEM analysis of the $RuCo_2O_4$ mesoporous nanoflakes (RCO100 sample): (a) Low-magnified TEM, (B) high magnified image presenting mesoporous feature (c) STEM image further confirming homogeneous distribution of nano-particles, (d) HRTEM image with corresponding lattice fringes and (e) SAED pattern.

Further, to get information regarding to the structure and surface features of the $RuCo_2O_4$ nanosheets (RCO100 sample) TEM measurements were carried out and presented in Fig. 3. As observed in Fig. 3 (a), the $RuCo_2O_4$ exhibits interconnected nanoflakes with a smooth surface. Impressively, the closer observation showed that these nanoflakes are decorated with the interconnected nanoparticles of around 8-10 nm in size which creates great inter-particles pores as seen from Fig. 3 (b-d). The uniform arrangement nanoparticles network in order to form continuous flakes is further confirmed by STEM image (Fig. 3c). This unique meso-porous

architecture provides an additional space and surplus electrochemically active sites for charge storage and intimate contact in between the electrode and electrolyte (S.I. S4). The HRTEM image of $RuCo_2O_4$ nanoflakes shows lattice with ineterplanner spacing ca. 2.45 and 2.91 Å which corresponds to (311) and (220) planes of $RuCo_2O_4$, respectively (Fig. 3 (d)). For detailed observations see supporting information (S.I. S5). The diffraction pattern shown in Fig. 3 (e) reveals clear diffraction circles, suggesting polycrystalline nature of $RuCo_2O_4$. In addition, the mesoporosity in the ultrathin nanoflakes is originated due to inter-particle spaces formed during the thermal treatments (Fig. 3d). These unique mesoporous nanoflakes can facilitate smother way for the electrolyte ion-transportation in the electrode material as well as improves the contact area for electrolyte ions to perform the rapid surface redox reactions.

Fig. 4 (a) shows the nitrogen adsorption/desorption isotherm for $RuCo_2O_4$ thin film prepared at 100 mV/s (RCO100). The type IV isotherm is observed and which imply the materialization of mesoporous $RuCo_2O_4$ nanoflakes. The calculated Brunauer-Emmett-Teller (BET) specific surface area for RCO100 sample is the 119 m^2/g, while the pore volume, and average pore width of $RuCo_2O_4$ nanoflakes are 0.26 cm^3/g, and 6.2 nm, respectively. The pore size distribution curve shows a maximum in the range 2 to 4 nm, providing an ideal pore size for large electrochemically active sites and enormous channels for ion transportation [40, 41]. This mesoporous structure of ultrathin $RuCo_2O_4$ nanoflakes provides small diffusion lengths as well as super-highway for electrolyte ion transportation [42]. The porosity in $RuCo_2O_4$ samples may originate from the internal spaces between interconnected mesoporous nanoflakes and inter-particle spaces. The narrow pore size distribution of $RuCo_2O_4$ sample further confirms uniform mesoporous surface morphology. Thus, by controlling the deposition scan rate for $RuCo_2O_4$ thin films we have tuned the surface morphology which alters the specific surface area of the thin film and is expected to show analogous effect on the electrochemical properties.

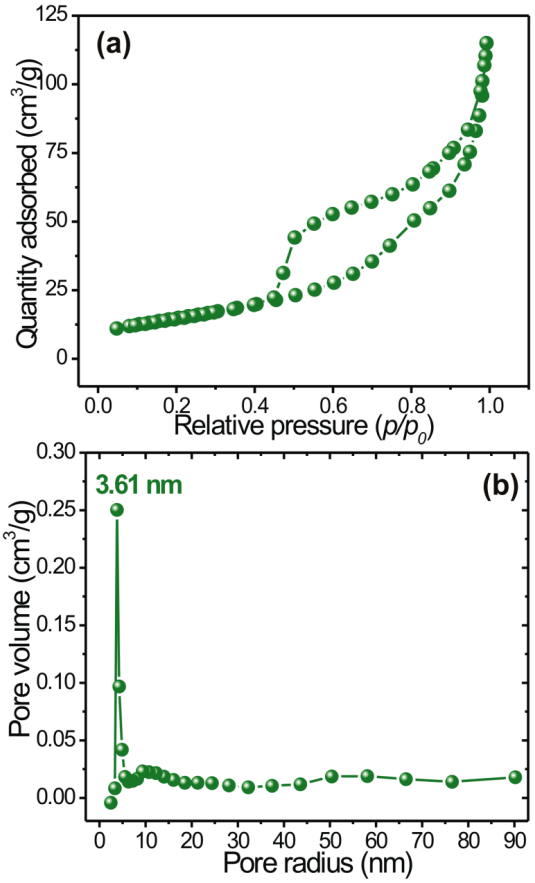

Fig. 4 (a) The nitrogen adsorption/desorption isotherms with (b) corresponding pore size distribution curve for RCO100 sample.

Subsequently, we directly applied the marigold-like $RuCo_2O_4$ mesoporous nanoflakes as a binder-free supercapacitive electrode as a working electrode in a three-electrode arrangement in 2 M KOH electrolyte. The CV profiles for three $RuCo_2O_4$ thin films (RCO25, RCO50 and RCO100) at a constant scan rate of 40 mV/s is presented in Fig. 5 (a). The operating voltage window for $RuCo_2O_4$ is from -0.4 to +0.4 V (vs Ag/AgCl) as applied elsewhere with ruthenium and cobalt based materials. For instance, Li et al. [43] tested supercapacitive properties of $RuO_2.xH_2O$/carbon aerogel in 6 M KOH between -1.0 V to 0.0 V (vs Hg/HgO) while Feng et al. [44] reported the operating potential range of -0.8 to +0.4 V (vs SCE) in the same electrolyte. Moreover, Wang et al. [45] used -0.4 to +0.4 V (vs Hg/HgO) potential window for RuO_2/TiO_2

nanocomposite. Similarly, for cobalt-based supercapacitor electrodes, the most widely used potential range is from -0.2 to +0.5 V (vs. Hg/HgO) [46, 47]. These reports suggest that the window we have chosen is perfectly suitable for the redox transitions of both Ru and Co materials.

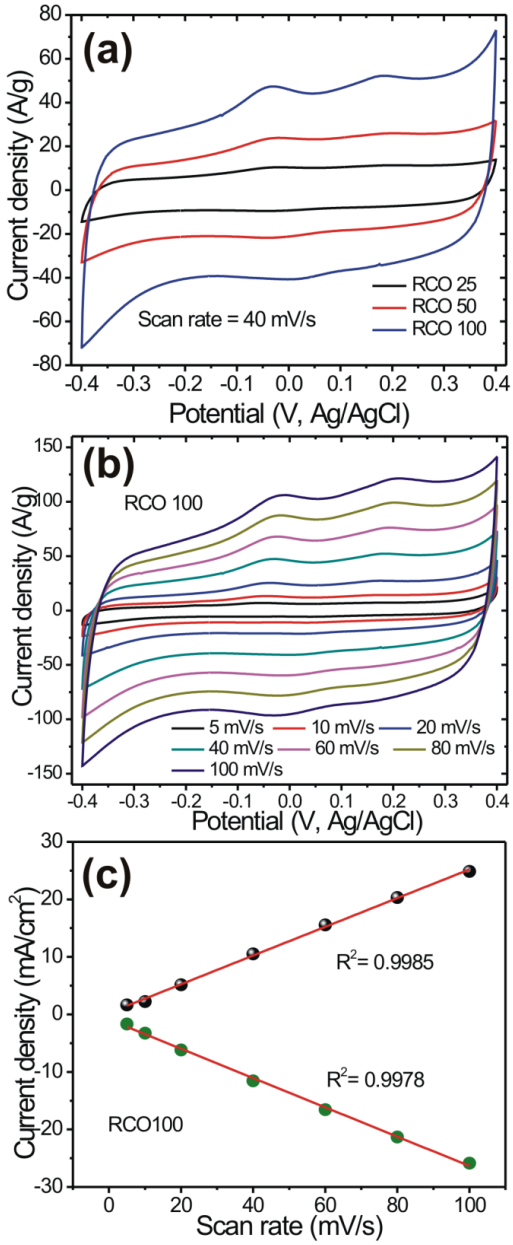

Fig. 5 (a) The CV profiles for all $RuCo_2O_4$ electrodes at 40 mV/s scan rate of in 2 M KOH electrolyte. (b) CV profiles for RCO100 sample at various scan rates from 5-100 mV/s and (c) The plot of anodic and cathodic current with respect to scan rate.

Further, the broad redox peaks along with box-shaped CV curves are clearly observed for $RuCo_2O_4$ samples which originate from the surface redox reactions i.e. pseudo-capacitance. The box-shaped CV curves further suggest extremely reversible redox transitions of $RuCo_2O_4$ which satisfies high-power condition in supercapacitors. Thus, the ideal rectangular shape with prominent redox peaks confirms the existence of Faradaic/pseudo-capacitive charge storing mechanism. The possible charge storing mechanism of $RuCo_2O_4$ in basic electrolyte will be as follows:

$$RuCo_2O_4 + OH^- + H_2O \Leftrightarrow RuOOH + 2CoOOH + 2e^- \quad (4)$$

Remarkably, the area under the curve in CV greatly increased for the RCO100 marigold-like architecture, leading to improved pseudo-capacitance which may be attributed to the efficient utilization of the $RuCo_2O_4$ ultrathin mesoporous nanoflakes. Further, Fig. 5 (b) presents the CV curves for RCO100 sample at various scan rates. The CV curves maintains their shape at higher as well as lower scan rate, signifying good rate-capability of unique marigold-like nanostructure (see S. I. S6 for CV curves of RCO25 and RCO50). Furthermore, slight shift in the anodic and cathodic peaks is observed with scan rate. Fig. 5 (c) illustrates the plot of current density (anodic and cathodic) versus the scan rate. From the figure it is observed that, the anodic and cathodic current linearly increased with the scan rate for RCO100 samples which further suggests facile charge transfer for open porous RCO100 sample.

The charge-discharge curves for all three $RuCo_2O_4$ samples at a current density of 6.6 A/g is shown in Fig. 6 (a). The outlines of charge-discharge curves are nearly symmetric for all $RuCo_2O_4$ samples, suggesting the Faradaic/pseudo-capacitive charge-storing mechanism with high reversibility for redox reactions in the whole potential region. Moreover, the initial small potential drop during the discharge corresponds to the intrinsic resistance of the material. Interestingly, RCO100 sample shows relatively low potential drop which can be associated with the ultrathin and open nanostructure of electrode material, leading to easy ion-diffusion and

enhanced electrochemical activity. Notably, RCO100 exhibits relatively longer discharge time than that for RCO25 and RCO50 electrodes at same current density, suggesting improved pseudo-capacitance due to porous mesoporous nanoflakes network. The specific capacitance during the charge-discharge process is estimated by applying the following equation:

$$C = \frac{I \cdot \int V \cdot dt}{m \cdot V^2} \qquad (5)$$

where I is the discharge current (A), Δt is the discharge time (sec), m is the mass of the active material (0.29-0.31 mg/cm^2) and ΔV is the potential window (V). The observed maximum specific capacitances for RCO25, RCO50 and RCO100 are found to be 351.4 F/g (105.4 mF/cm^2), 773.2 F/g (231.9 mF/cm^2) and 1469.2 F/g (440.7 mF/cm^2), respectively (Fig. 6 (c)).

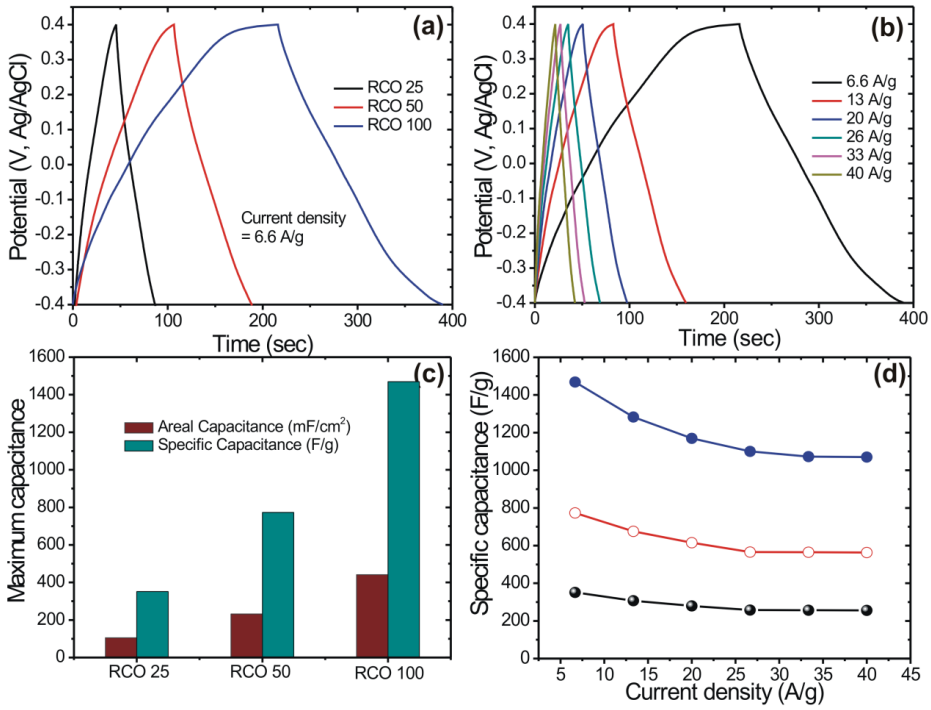

Fig. 6 (a) charge-discharge curves for $RuCo_2O_4$ electrodes at 6.6 A/g in 2 M KOH electrolyte. (b) charge-discharge curves for the RCO100 sample at current densities of 6.6, 13, 20, 26, 33, 40 A/g (c) the comparison of specific and areal capacitances for RCO25, RCO50 and RCO100 samples and (d) plot of specific capacitance with current density for RCO25, RCO50 and RCO100 samples.

Thus, an extensive upsurge in the capacitance is observed by simply changing the deposition scan rate and consequently the altered surface morphology from compact nano-petals to 3D network of ultrathin mesoporous nanoflakes prominently increase the energy storing capacity of the electrode (S.I. S7). The observed specific capacitance for $RuCo_2O_4$ electrode in the present work is considerably higher than that for electrodeposited Ru- and Co-based supercapacitor electrodes. For example, Jagadale et. al. [48] reported a specific capacitance of 890 F/g for potentiodynamically deposited $Co(OH)_2$ mesoporous nanoflakes. With the same method, urea-doped cobalt hydroxide mesoporous nanoflakes were prepared by Vinothbabu et al. [49], on stainless steel and achieved a highest specific capacitance of 1200 F/g at 0.5 mA current density. Recently, Patil and coworkers [50] grew $Co(OH)_2$ microflakes on 3D graphene foam in potentiodynamic mode at 50 mV/s scan rate and observed maximum specific capacitance of 1030 F/g at current density of 9.09 A/g. Similarly, 1000 F/g specific capacitance is reported for the Ru-based supercapacitors [51-53]. Moreover, the specific capacitance value for $RuCo_2O_4$ is comparable and even higher as compared to that reported elsewhere for MTMOs nanostructures (see Table S.I. S7).

The higher rate capability is the fundamental requirement of the energy storage devices. For that the electrode must conserve their electrochemical performance at lower as well as higher scanning rate. Hence, the specific capacitance is calculated at various current densities for all $RuCo_2O_4$ samples and plotted in the Fig. 6 (d) as a function of current density. The $RuCo_2O_4$ electrode (RCO100 sample) establishes the superior rate capability by keeping initial 72.8 % capacitance at 40 A/g current density (from 1469.1 to 1070 F/g). The credit for this noteworthy rate capability goes to ultrathin mesoporous $RuCo_2O_4$ nanoflakes which can provide the smother and short diffusion path for electrolyte ions and stimulates fast surface redox reactions.

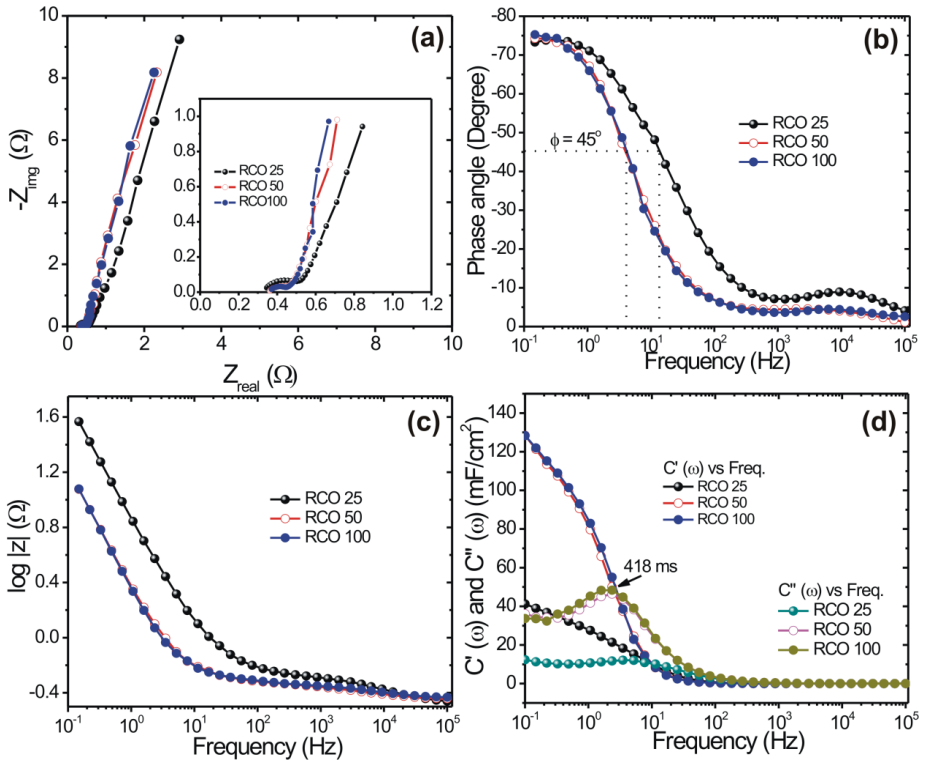

Fig. 7 (a) Nyquist plot of $RuCo_2O_4$ electrodes with enlarged view in the inset within a frequency range of 0.1 Hz to 10^5 Hz (b) plot of log f vs. phase angle (ϕ) (c) log f vs. log|Z| and (d) real and imaginary capacitances (C' and C") vs. frequency (log f) of $RuCo_2O_4$ thin films

Nyquist plots for RCO25, RCO50 and RCO100 are shown in Fig. 7 (a). Generally, Nyquist plot is separated into two major regions such as high and low-frequency region. The high frequency region corresponds for the interfacial processes while the low-frequency region is associated with the capacitive behavior. The high-frequency region associated with the very small semicircle for all $RuCo_2O_4$ samples suggesting a low charge transfer resistance. The RCO100 sample shows relatively small charge transfer resistance than that for RCO50 and RCO25 because of the open porous nanostructure which allows easy access for ions. The Nyquist plot aligned in the straight line for RCO100 and RCO50 samples in the low-frequency region representing an ideal capacitive behavior which suggesting the mesoporous nanoflakes have better capacitor behavior than immature or thick nano-petal-like $RuCo_2O_4$ (RCO25). The

electrolyte resistance (R_s) encompassing all Ohmic contributions is almost the same for all the samples at 0.34 Ω, indicating a low internal resistance (ESR, see inset of Fig. 7(a)). Furthermore, the RCO100 electrode showed the smallest semicircle which signifies its lower charge-transfer resistance and excellent capacitive nature as compared to the RCO50 and RCO25 electrodes. Thus, $RuCo_2O_4$ mesoporous nanoflakes lead to reduced charge transfer resistance, which might be the reason for enhancement in the electrochemical performance. Fig. 7 (b) presents the phase angles of $RuCo_2O_4$ electrodes which are close to 90°, revealing an ideal capacitor performance [54]. Moreover, the ideal capacitive behavior of the electrode is to estimate the frequency at which the phase angle crosses 45° angle [55]. For example, the commercial activated carbon based EDLCs shows a 45° phase angle at the frequency of ~0.2 Hz [56]. In the present investigation, the $RuCo_2O_4$ (RCO100) electrodes show the phase angle of 45° at a frequency of ~4 Hz, suggesting a rapid frequency response and excellent capacitive behavior. Interestingly, as morphology changed from thick nano-petals (RCO25) to open porous 3D network of mesoporous nanoflakes (RCO100 or RCO50), this frequency is also lowered down from ~13 to ~4 Hz, suggesting more capacitive behavior for mesoporous nanoflakes. As seen from Fig. 7 (c), the frequency dependent impedance decreased from RCO25 to RCO100 sample, which signifies the enhanced conductivity of the $RuCo_2O_4$ electrode [57]. Here, the RCO electrode reaches the frequency independent impedance already at low frequencies in the following order RCO100 (~11.2 Hz) < RCO50 (~11.5 Hz) < RCO25 (~80.2 Hz), demonstrating that the RCO100 electrode allows the higher surface for ionic diffusion as compared to the other $RuCo_2O_4$ electrodes. Furthermore, the capacitive behavior of $RuCo_2O_4$ can also be evaluated from EIS technique by calculating the real and imaginary capacitance at a corresponding frequency using following equations:

$$C(\omega) = C'(\omega) - jC''(\omega) \qquad (6)$$

Where, $C^{'}(\omega) = \frac{Z^{''}(\omega)}{\omega \mid Z(\omega) \mid^2}$ (7)

$$C^{''}(\omega) = \frac{Z^{'}(\omega)}{\omega \mid Z(\omega) \mid^2} \quad (8)$$

where '*Z'* the complex impedance represented as $Z(\omega) = Z'(\omega) + Z''(\omega)$ and $\omega = 2\pi f$ where *f* is the frequency. *C*' (ω) is the real accessible capacitance of the electrode while *C*" (ω) is the energy loss due to the irreversible processes of the electrodes, *Z*' and *Z*" are the real and imaginary parts of the Nyquist plot, respectively. The complex AC capacitance at different frequencies for $RuCo_2O_4$ electrodes is shown in Fig. 7 (d). The plot shows common relaxation-type dispersions where the real capacitance 'C' reduces with frequency while 'C"' shows maxima. The relaxation time constant was evaluated using the following relation ($\tau_0 = 1/f_0$), which was found to be 418 ms for RCO100 and RCO50 electrodes. This value was found to be lower than that for other carbon electrodes, for instance activated carbon (τ_0=700 ms) [58].

Furthermore, the cycling stability of the $RuCo_2O_4$ mesoporous nanoflakes is investigated by measuring the charge-discharge cycles at current density of 13, 20, 26, 33, and 40 A/g. Fig. 8 displays the plot of specific capacitance versus the cycle number for RCO100 electrode. At current density of 13 A/g the electrode shows the specific capacitance of 1284.2 F/g (for the first cycle) and it is decreased to 1182.3 F/g with 91.3 % retention after 3000 cycles. Moreover, these $RuCo_2O_4$ electrodes show high rate capability. The specific capacitances of the electrode is calculated for each current densities of 13, 20, 26, 33 and 40 A/g, after completing the 500 cycles for each current density. The observed specific capacitances are 1284.2, 1174, 1080.4, 1043.6, and 1030.2 F/g at current densities of 13, 20, 26, 33 and 40 A/g, respectively. A recovered specific capacitance of 1182.3 (91.3 % of the initial capacitance) can be calculated for the next 500 cycles without any further decrease when the current density tuned back to 13

A/g. The results imply that the unique combination and smart design of $RuCo_2O_4$ obtained by potentiodynamic deposition significantly boosted the electrochemical properties.

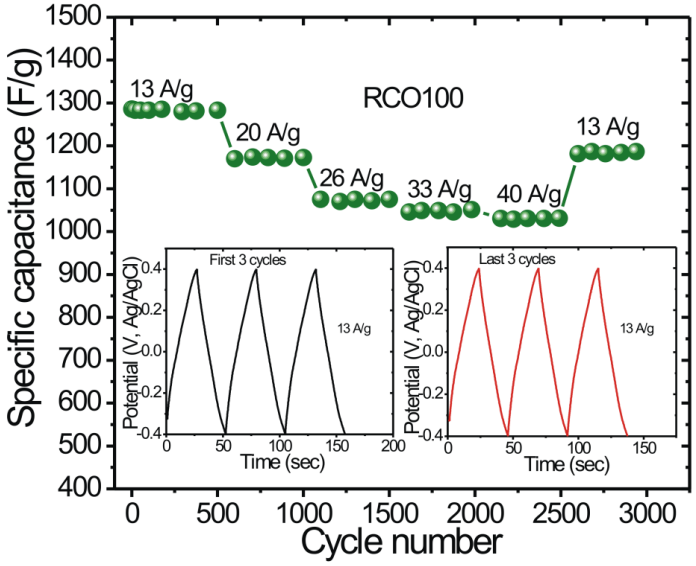

Fig. 8 cycling performance of the $RuCo_2O_4$ electrode (RCO100) by GCD at gradual increasing current densities. Inset figures shows the first and last three GCD cycles

The two electrode measurements are always preferred for getting the true electrochemical performance of the supercapacitive electrode. For that, we have assembled the aqueous asymmetric supercapacitor (after balancing the charge of both electrode) using the RCO100 (positive electrode) and AC (negative electrode) in the optimized 2 M KOH electrolyte. The CV profiles for $RuCo_2O_4$//AC asymmetric supercapacitor at scan rate of 5, 10, 20, 40, 60, 80 and 100 mV/s within voltage limit of 0 to 1.4 V is shown in Fig. 9 (a). The presented CV profiles shows the nearly rectangular shape and it is maintained at higher scan rate also suggesting the $RuCo_2O_4$//AC asymmetric supercapacitor have better supercapacitive features. Likewise, the charge-discharge curves for the $RuCo_2O_4$//AC asymmetric supercapacitor device at current densities of 0.6, 1.2, 2.4, 3.5, 4.7 A/g is given in the Fig. 9 (b). At lower current density, the discharge curve clearly shows the non-linear behavior with the charge curves, which is due to the redox reactions of the $RuCo_2O_4$ electrode material. Moreover, the increasing

current density shrinks the discharging time. This is because of at higher current density all the electroactive sites of electrodes are not reachable for electrolyte ions that will reduce the charge storing capacity of the supercapacitor.

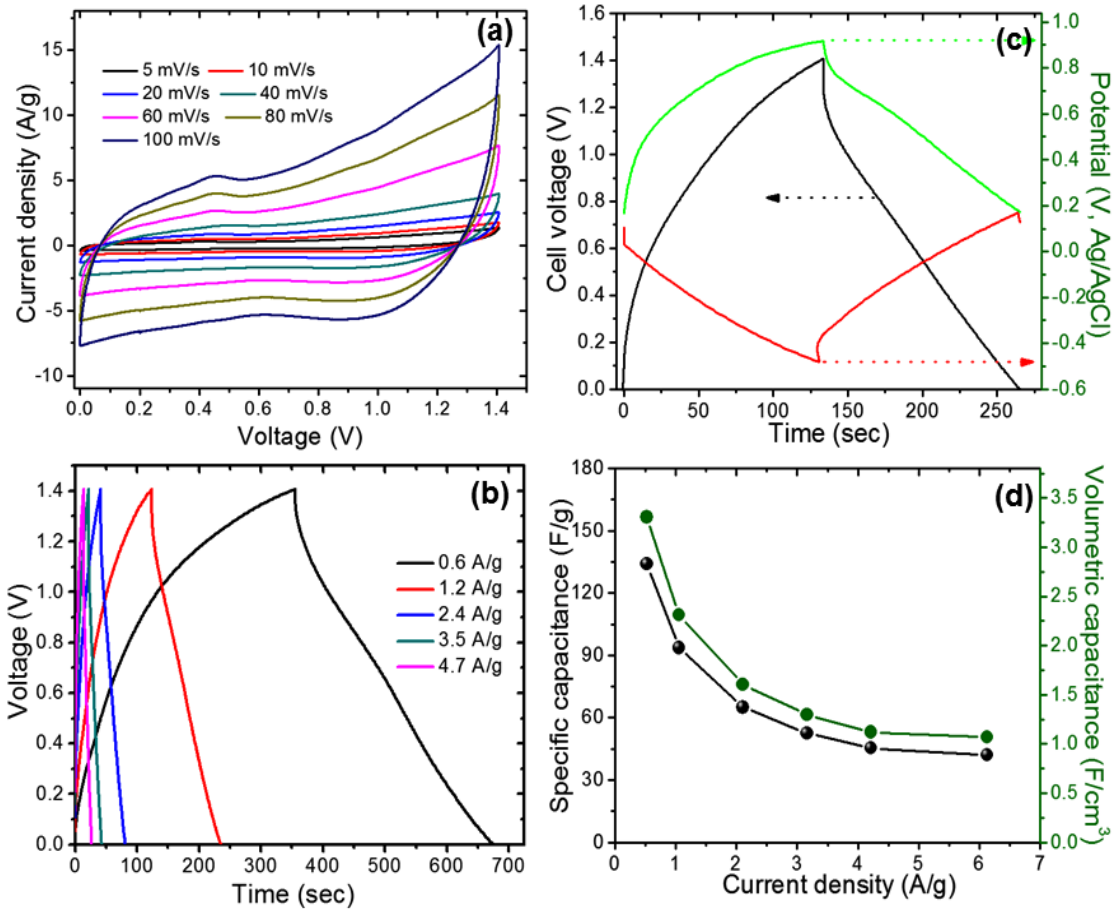

Fig. 9 (a) CV and (b) charge-discharge profiles for $RuCo_2O_4$//AC asymmetric supercapacitor at various scanning rates, (c) representative charge-discharge curves at current density of 1.2 A/g for $RuCo_2O_4$//AC asymmetric supercapacitor and (d) the variation of the specific and volumetric capacitance with current density for $RuCo_2O_4$//AC asymmetric supercapacitor

To get more information regarding to the contribution of RCO100 and AC electrodes in charge storage the representative charge-discharge measurement carried out at 1.2 A/g current density as shown in Fig. 9 (c). As seen in the figure, both the electrodes contribute equal potential for charge storing. The negative electrode actively contributes the charge storage in the voltage

limit of 0 to 0.8 V, while the positive electrode contributes the potential form the 0.8 to 1.4 V. By considering the total mass of electrode material and volume of the whole cell, the specific and volumetric capacitance are calculated for the $RuCo_2O_4$//AC asymmetric supercapacitor device. Fig. 9 (d) represents the plot of capacitance (specific and volumetric) as a function of the current density for $RuCo_2O_4$//AC asymmetric supercapacitor. The $RuCo_2O_4$//AC asymmetric supercapacitor device offers the volumetric capacitance of 3.3 F/cm^3 (133 F/g) at lower current density of 0.6 A/g. Notably, the better rate capability is observed for the $RuCo_2O_4$//AC asymmetric supercapacitor devices as it sustains 34 % by initial volumetric capacitance of even at higher current density of 4.7 A/g.

For the energy storage device, the energy storing capacity and the energy delivering ability are very essential to decide the usefulness of the assembled device for practice purpose. Therefore, we calculated specific energy and power for $RuCo_2O_4$//AC asymmetric supercapacitor device by considering the discharging time and it is plotted in the Ragone plot (Fig. 10 (a). Our assembled $RuCo_2O_4$//AC asymmetric supercapacitor device shows the maximum specific energy of 36.5 Wh/kg with maximum specific power of 3294 W/kg. The obtained values of specific energy and power are comparable to the values reported for NiCo2O4 electrodes [59-67]. The excellent electrochemical performance for $RuCo_2O_4$//AC asymmetric supercapacitor device in terms of higher specific capacitance and specific energy originate from the higher electrical conductivity of both the electrodes and extended operating potential window of the asymmetric supercapacitor device. In addition, the supercapacitors are well known for their long-term cycling stability that why in may advance electronic gadgets supercapacitors are preferred as an energy storage device. Therefore, it is very essential to measure the cycling stability of the assembled asymmetric supercapacitor device. The stability test is carried out by running the 2500 charge-discharge cycles at current density of 2.4 A/g for the $RuCo_2O_4$//AC asymmetric supercapacitor device. Fig. 10 (b) present the plot of coulombic efficiency and capacitance retention with cycle number. About 82 % of the initial capacitance is

maintained by the device after 2500 cycles demonstrating the better cycling stability. The decay in the capacitance may be observed due to the aggregation of the active electrode material during the repeatedly charge-discharge cycles. More importantly, the $RuCo_2O_4$//AC asymmetric supercapacitor device shows the 97 % Coulombic efficiency even after 2500 charge-discharge cycles presenting excellent supercapacitive features of the device. Thus, the above discussed electrochemical results indicating the best capabilities of the novel $RuCo_2O_4$ thin film for high performance supercapacitor application. The credit of excellent electrochemical performance for the asymmetric supercapacitor device goes to (i) the ultrathin mesoporous nanoflakes composed nanostructure of the RCO100 thin film provide small ionic diffusion path which results in fast surface redox reactions and excellent rate capability; (ii) the pores in between the mesoporous nanoflakes will further increase the electrochemically active surface area and (III) the complimentary potential windows of RCO100 and AC electrodes helps for extending the voltage of the device and finally IV) the nanostructure is supported on stainless steel substrate which avoids the use of unnecessary additives, consequently, no inactive materials are needed.

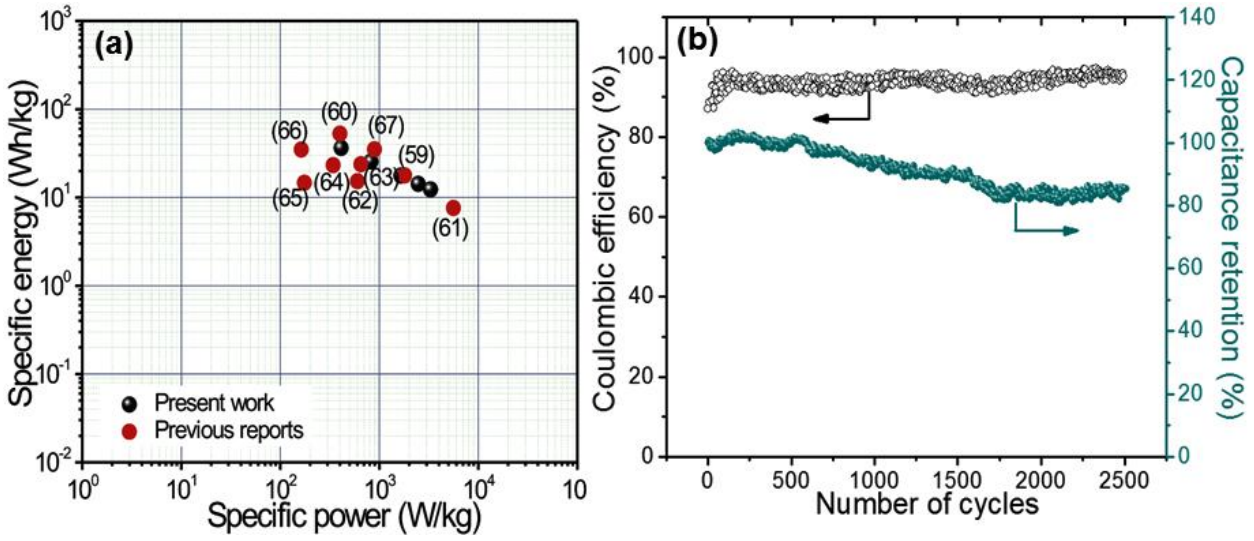

Fig. 10 (a) Ragone plot for $RuCo_2O_4$//AC asymmetric supercapacitor device and (b) the plot of coulombic efficiency and capacitance retention with cycle numbers.

Conclusions

In conclusion, a very simple but proficient electrochemical method is used to prepare a novel nanostructured $RuCo_2O_4$ mesoporous nanoflakes with high supercapacitive performance. This novel pseudo-capacitive $RuCo_2O_4$ nanoflakes electrode ultrahigh specific capacitance (1469 F/g) with brilliant long-lasting cycling stability up to 3000 charge-discharge cycles (90.2 % capacity retention after 3000 cycles). Further, the synergistic combination of the $RuCo_2O_4$ and AC electrode in asymmetric design prolong the operating potential range of the cell to 1.4 V with higher specific energy of 32.63 Wh/kg (1.1 mWh/cm^3). Such a fascinating supercapacitive features of the asymmetric cell is credited to the unique 3D network of hierarchical mesoporous nanoflakes and the conductive $RuCo_2O_4$ with low series and charge transfer resistances. Therefore, this work ensures the importance of coherent design of an innovative nanostructured design of electrode materials for supercapacitors.

Acknowledgement

DPD and PGR appreciate the award with the support of the Secretary for Universities and Research of the Ministry of Economy and Knowledge of the Government of Catalonia and the Co-fund program of the Marie Curie Actions of the 7th R&D Framework Programme of the European Union. DPD and PGR also acknowledge AGAUR (Generalitat de Catalunya) for Project NESTOR (Nanomaterials for Energy STORage) 2014_SGR_1505.

References

[1] Dubal, D. P.; Gomez-Romero, P.; Sankapal, B. R.; Holze, R.; Nickel cobaltite as an emerging material for supercapacitors: An overview. *Nano Energy*, **2015**, 11, 377-399.

[2] Yuan, C.; Wu, H. B.; Xie, Y.; Lou, X. W.; Mixed Transition-Metal Oxides: Design, Synthesis, and Energy-Related Applications**.** *Angew. Chem. Int. Ed.* **2014**, 53, 1488-1504.

[3] Zhang, Y.; Li, L.; Su, H.; Huang, W.; Dong, X.; Binary metal oxide: advanced energy storage materials in supercapacitors. *J. Mater. Chem. A*, **2015**, 3, 43-59.

[4] Dubal, D. P.; Ayyad, O.; Ruiz, V.; Gomez-Romero, P.; Hybrid energy storage: the merging of battery and supercapacitor chemistries. *Chem. Soc. Rev.,* **2015**, 44, 1777-1790.

[5] Zhou, L.; Zhao, D.; Lou, X. W.; Double-Shelled $CoMn_2O_4$ Hollow Microcubes as High-Capacity Anodes for Lithium-Ion Batteries. *Adv. Mater.* **2012**, 24, 745-748.

[6] Wei, T. Y.; Chen, C. H.; Chien, H. C.; Lu, S. Y.; Hu, C. C.; A Cost-Effective Supercapacitor Material of Ultrahigh Specific Capacitances: Spinel Nickel Cobaltite Aerogels from an Epoxide-Driven Sol–Gel Process. *Adv. Mater.* **2010**, 22, 347-351.

[7] Zhang, G.; Yu, L.; Wu, H. B.; Hoster, H. E.; Lou, X. W.; Formation of $ZnMn_2O_4$ Ball-in-Ball Hollow Microspheres as a High-Performance Anode for Lithium-Ion Batteries. *Adv. Mater.* **2012**, 24, 4609-4613.

[8] Teh, P. F.; Sharma, Y.; Pramana, S. S.; Srinivasan, M.; Nanoweb anodes composed of one-dimensional, high aspect ratio, size tunable electrospun $ZnFe_2O_4$ nanofibers for lithium ion batteries. *J. Mater. Chem.* **2011**, 21, 14999-15008.

[9] Zhang, G.; Lou, X. W.; Controlled growth of $NiCo_2O_4$ nanorods and ultrathin nanosheets on carbon nanofibers for high-performance supercapacitors. *Sci. Rep.*, **2013**, 3, 1470.

[10] Jiang, H.; Ma, J.; Li, C. Z.; Hierarchical porous $NiCo_2O_4$ nanowires for high-rate supercapacitors. *Chem. Commun.*, **2012**, 48, 4465-4467.

[11] Deng, D. H.; Pang, H,; Du, J. M.; Deng, J. W.; Li, S. J.; Chen, J.; Zhang, J. S.; Fabrication of cobalt ferrite nanostructures and comparison of their electrochemical properties. *Cryst. Res. Technol.*, **2012**, 47, 1032-1038.

[12] Zhang, M.; Guo, S. H.; Zhang, G. N.; Hao, Z. P.; Kang, L. P.; Liu, Z. H.; Preparation of $NiMn_2O_4$ with large specific surface area from an epoxide-driven sol−gel process and its capacitance. *Electrochim. Acta*, **2013**, 87, 546-553.

[13] Lu, Q.; Chen, J. G.; Xiao, J. Q.; Nanostructured Electrodes for High-Performance Pseudocapacitors. *Angew. Chem. Int. Ed.* **2013**, 52, 1882-1889.

[14] Wang, G.; Zhang, L.; Zhang, J.; A review of electrode materials for electrochemical supercapacitors. *Chem. Soc. Rev.* 2012, **41**, 797-828.

[15] Courtel, F. M.; Duncan, H.; Abu-Lebdeh, Y.; Davidson, I. J.; High capacity anode materials for Li-ion batteries based on spinel metal oxides AMn_2O_4 (A ¼ Co, Ni, and Zn). *J. Mater. Chem.* **2011**, 21, 10206-10218.

[16] Anwar, S.; Muthu, K. S.; Ganesh, V.; Lakshminarasimhan, N.; A comparative study of electrochemical capacitive behavior of $NiFe_2O_4$ synthesized by different routes *J. Electrochem. Soc.* 2011, **158**, A976-A981.

[17] Sun, S.; Wen, z.; Jin, J.; Cui, Y.; Lu, Y.; Synthesis of ordered mesoporous $CuCo_2O_4$ with different textures as anode material for lithium ion battery, *Microporous Mesoporous Mater.* **2013**, 169, 242- 247.

[18] Bahlawane, N.; Ngamou, P. H. T.; Vannier, V.; Kottke, T.; Heberle, J.; Kohse-Hoeinghaus, K.; Tailoring the properties and the reactivity of the spinel cobalt oxide. *Phys. Chem. Chem. Phys.* **2009**, 11, 9224-9232.

[19] Sharma, Y.; Sharma, N.; Rao, G. V. S.; Chowdari, B. V. R.; Studies on spinel

cobaltites, FeCo2O4 and MgCo2O4 as anodes for Li-ion batteries. *Solid State Ionics* **2008**, 179, 587-597.

[20] Fei, J. B.; Cui, Y.; Yan, X. H.; Qi, W.; Yang, Y.; Wang, K. W.; He, Q.; Li, J. W.; Controlled Preparation of MnO_2 Hierarchical Hollow Nanostructures and Their Application in Water Treatment. *Adv. Mater.*, **2008**, 20, 452-456.

[21] Sun, G. B.; Dong, B. X.; Cao, M. H.; Wei, B. Q.; Hu, C. W.; Hierarchical Dendrite-Like Magnetic Materials of Fe_3O_4, γ-Fe_2O_3, and Fe with High Performance of Microwave Absorption. *Chem. Mater.*, **2011**, 23, 1587-1593.

[22] Wang, B.; Chen, J. S.; Wu, H. B.; Wang, Z. Y.; Lou, X. W.; Quasiemulsion-Templated Formation of α-Fe_2O_3 Hollow Spheres with Enhanced Lithium Storage Properties. *J. Am. Chem. Soc.*, 2011, **133**, 17146-17148.

[23] Rechnitz G. A.; Goodkin, S. C.; Some Properties of Ruthenium (III) and (IV) in Acid Solution. *Platinum Metals Rev.*, **1963,** 7, 26.

[24] Bard, A. J.; Parsons, R.; Jordan, J.; "Standard Potentials in Aqueous Solutions", Marcel, Dekker, New York, **1985**, pp-413-421.

[25] Hansal, W. E. G.; Tury, B.; Halmdienst, M.; Varsanyi, M. L.; Kautek, W.; Pulse reverse plating of Ni–Co alloys: Deposition kinetics of Watts, sulfamate and chloride electrolytes. *Electrochim. Acta*, **2006**, 52, 1145-1151.

[26] Sudha, V.; Sangaranarayanan, M. V.; Underpotential Deposition of Metals: Structural and Thermodynamic Considerations. *J. Phys. Chem. B*, **2002**, 106, 2699-2707.

[27] Jagadale, A. D.; Jamadade, V. S.; Pusawale, S. N.; Lokhande, C. D.; Effect of scan rate on the morphology of potentiodynamically deposited beta-Co(OH)(2) and corresponding supercapacitive performance. *Electrochim. Acta*, **2012**, 78, 92-97.

[28] Thorogood, G. J.; Zhang, Z.; Hester, J. R.; Kennedy, K. J.; Ting, J.; Gloverd, C. J.; Johannessen, B.; Structure and cation ordering in spinel-type $TcCo_2O_4$. An example of

a trivalent technetium oxide. *Dalton Trans.*, 2011, **40**, 10924-10926.

[29] Morgan, D. J.; Resolving Ruthenium: XPS Studies of Common Ruthenium Materials. *Surf. Interface Anal.* 2015, **47**, 1072-1079.

[30] Kötz, R.; XPS Studies of Oxygen Evolution on Ru and RuO_2 Anodes. *J. Electrochem. Soc.* **1983**, 130, 825-829.

[31] Shen, J. Y.; Adnot, A.; Kaliaguine, S.; An ESCA study of the interaction of oxygen with the surface of ruthenium. *Appl. Surf. Sci.* **1991**, 51, 47-60.

[32] Saveleva, V. A.; Wang, L.; Luo, W.; Zafeiratos, S.; Ulhaq-Bouillet, C.; Gago, A.; Andreas, F. K.; E. R. Savinova, Uncovering the Stabilization Mechanism in Bimetallic Ruthenium–Iridium Anodes for Proton Exchange Membrane Electrolyzers. *J. Phys. Chem. Lett.*, **2016**, 7, 3240–3245.

[33] Atanasoska, L.; Grady, W.; Atanasoski, R. T.; Pollak, F.; The surface structure of RuO_2: A leed, auger and XPS study of the (110) and (100) faces. *Surf. Sci.* **1988**, 202, 142-166.

[34] Cox, P. A.; Goodenough, J. B.; Tavener, P. J.; Telles, D.; Egdell, R. G.; The electronic structure of $Bi_2{-}xGdxRu_2O_7$ and RuO_2: A study by electron spectroscopy. *J. Solid State Chem.* **1986**, 62, 360-370.

[35] Lü, M.; Deng, X.; Waerenborgh, J. C.; Wu, X.; Meng, J.; Redox chemistry and magnetism of $LaSrM_{0.5}Ru_{0.5}O_{4\pm\delta}$ (M = Co, Ni and Zn) Ruddlesden–Popper phases. *Dalton Trans.*, 2012, **41**, 11507-11518.

[36] Yuan, C.; Li, J.; Hou, L.; Zhang, X.; Shen, L.; Lou, X. W.; Ultrathin Mesoporous $NiCo_2O_4$ Nanosheets Supported on Ni Foam as Advanced Electrodes for Supercapacitors. *Adv. Funct. Mater.* **2012**, 22, 4592-4597.

[37] Khalid, S.; Cao, C.; Ahmad, A.; Wang, L.; Tanveer, M.; Aslam, I.; Tahir, M.; Idrees, F.; Zhu, Y.; A high performance solid state asymmetric supercapacitor device based upon

$NiCo_2O_4$ nanosheets//MnO_2 microspheres. *RSC Adv.*, **2015**, 5, 33146-33154.

[38] Roginskaya, Y. E.; Morozova, O. V.; Lubnin, E. N.; Ulitina, Y. E.; Lopukhova, G. V.; Trasatti, S.; Characterization of Bulk and Surface Composition of $Co_xNi_{1-x}Oy$ Mixed Oxides for Electrocatalysis. *Langmuir* **1997**, 13, 4621-4627.

[39] Dubal, D. P.; Holze, R.; Self-assembly of stacked layers of Mn_3O_4 nanosheets using a scalable chemical strategy for enhanced, flexible, electrochemical energy storage. *J. Power Sources* **2013**, 238, 274-282.

[40] Zhang, G. Q.; Wu, H. B.; Hoster, H. E.; Chan-Park, M. B.; Lou, X. W.; Single-crystalline NiCo2O4 nanoneedle arrays grown on conductive substrates as binder-free electrodes for high-performance supercapacitors. *Energ. Environ. Sci*., **2012**, 5, 9453-9456.

[41] Chen, Y.; Qu, B.; Hu, L.; Xu, Z.; Li, Q.; Wang, T.; High-performance supercapacitor and lithium-ion battery based on 3D hierarchical NH_4F-induced nickel cobaltate nanosheet–nanowire cluster arrays as self-supported electrodes. *Nanoscale*, **2013**, 5, 9812-9820.

[42] Xu, M. W.; Kong, L. B.; Zhou, W. J.; Li, H. L.; Hydrothermal Synthesis and Pseudocapacitance Properties of α-MnO_2 Hollow Spheres and Hollow Urchins. *J. Phys. Chem. C*, **2007**, 111, 19141-19147.

[43] Li, J.; Wang, X.; Huang, Q.; Dai, C.; Gamboa, S.; Sebastian, P. J.; Preparation and characterization of $RuO_2.xH_2O$/carbon aerogel composites for supercapacitors. *J. Appl. Electrochem.*, **2007**, 37, 1129-1135.

[44] Wang, X. F.; You, Z.; Ruan, D. B; A Hybrid Metal Oxide Supercapacitor in Aqueous KOH Electrolyte. *Chin. J. Chem.*, **2006**, 24, 1126-1132.

[45] Wang, Y. G.; Wang, Z. D.; Xia, Y. Y.; An asymmetric supercapacitor using RuO_2/TiO_2 nanotube composite and activated carbon electrodes. *Electrochim. Acta* **2005**, 50,

5641–5646.

[46] Wang, R.; Yan, X.; Lang, J.; Zheng, Z.; Zhang, P.; A hybrid supercapacitor based on flower-like $Co(OH)_2$ and urchin-like VN electrode materials. *J. Mater. Chem. A*, **2014**, 2, 12724-12732.

[47] Tummala, R.; Guduru, R. K.; Mohanty, P. S.; Nanostructured Co_3O_4 electrodes for supercapacitor applications from plasma spray technique. *J. Power Sources* **2012**, 209, 44-51.

[48] Jagadale, A. D.; Jamadade, V. S.; Pusawale, S. N.; Lokhande, C. D.; Effect of scan rate on the morphology of potentiodynamically deposited β-$Co(OH)_2$ and corresponding supercapacitive performance. *Electrochim. Acta* **2012**, 78, 92-97.

[49] Vinothbabu, P.; Elumalai, P.; Tunable supercapacitor performance of potentiodynamically deposited urea-doped cobalt hydroxide. *RSC Adv.*, **2014**, 4, 31219-31225.

[50] Patil, U. M.; Nam, M. S.; Sohn, J. S.; Kulkarni, S. B.; Shin, R.; Kang, S.; Lee, S.; Kim, J. H.; Jun, S. C.; Controlled electrochemical growth of $Co(OH)_2$ flakes on 3D multilayered graphene foam for high performance supercapacitors. *J. Mater. Chem. A*, 2014, **2**, 19075-19083.

[51] Bi, R. R.; Wu, X. L.; Cao, F. F.; Jiang, L. Y.; Guo, Y. G.; Wan, L. J.; Highly Dispersed RuO_2 Nanoparticles on Carbon Nanotubes: Facile Synthesis and Enhanced Supercapacitance Performance. *J. Phys. Chem. C*, **2010**, 114, 2448-2451.

[52] Gujar, T. P.; Kim, W. Y.; Puspitasari, I.; Jung, K. D.; Joo, O. S.; Electrochemically Deposited Nanograin Ruthenium Oxide as a Pseudocapacitive Electrode. *Int. J. Electrochem. Sci.,* **2007**, 2, 666-673.

[53] Park, B. O.; Lokhande, C. D.; Park, H. S.; Jung, K. D.; Joo, O. S.; Performance of supercapacitor with electrodeposited ruthenium oxide film electrodes—effect of film

thickness. *J. Power Sources* **2004**, 134, 148-152.

[54] Yuan, L. Y.; Lu, X. H.; Xiao, X.; Zhai, T.; Dai, J. J.; Zhang, F. C.; Hu, B.; Wang, X,; Gong, L.; Chen, J.; Hu, C.; Tong, Y.; Zhou, J.; Wang, Z. L.; Flexible solid-state supercapacitors based on carbon nanoparticles/MnO2 nanorods hybrid structure. *ACS Nano* **2012**, 6, 656-661.

[55] Hsia, B.; Marschewski, J.; Wang, S.; In, J. B.; Carraro, C.; Poulikakos, D.; Grigoropoulos, C. P.; Maboudian, R.; Highly flexible, all solid-state micro-supercapacitors from vertically aligned carbon nanotubes. *Nanotechnology*, **2014**, 25, 055401.

[56] Miller, J. R.; Outlaw, R. A.; *J. Electrochem. Soc.*, **2015**, 162, A507-A5082.

[57] Yuan, D.; Zheng, J.; Kristian, N.; Wang, Y.; Wang, X.; Bi_2O_3 deposited on highly ordered mesoporous carbon for supercapacitors. *Electrochem. Commun.*, **2009**, 11, 313-317.

[58] Huang, P.; Pech, D.; Lin, R.; McDonough, J. K.; Brunet, M.; Taberna, P. L.; Gogotsi, Y.; Simon, P.; On-chip micro-supercapacitors for operation in a wide temperature range. *Electrochem. Commun.*, **2013**, 36, 53-56.

[59] Hu, C. C.; Hsu, C. T.; Chang, K. H.; Hsu, H. Y.; Microwave-assisted hydrothermal annealing of binary Ni–Co oxy-hydroxides for asymmetric supercapacitors. *J. Power Sources* **2013**, 238, 180-189

[60] Wang, R.; Yan, X. Superior Asymmetric Supercapacitor based on Ni-Co Oxide Nanosheets and Carbon Nanorods. *Sci. Rep.* **2014**, *4*, 3712

[61] Wang, H.; Holt, C. M. B.; Li, Z.; Tan, X.; Amirkhiz, B. S.; Xu, Z.; Olsen, B. C.; Stephenson, T.; Mitlin, D. Graphene-Nickel Cobaltite Nanocomposite Asymmetrical Supercapacitor with Commercial Level Mass Loading. *Nano Res.* 2012, **5**, 605-617

[62] Lu, X. F.; Wu, D. J.; Li, R. Z.; Li, Q.; Ye, S. H.; Tong, Y. X.; Li, G. R. Hierarchical

$NiCo_2O_4$ Nanosheets@Hollow Microrod Arrays for High-performance Asymmetric Supercapacitors. *J. Mater. Chem. A*, **2014**, *2*, 4706-4713

[63] Chen, H.; Jiang, J.; Zhang, L.; Qi, T.; Xia, D.; Wan, H. Facilely Synthesized Porous $NiCo_2O_4$ Flowerlike Nanostructure for High-rate Supercapacitors. *J. Power Sources*, **2014**, *248*, 28-36

[64] Wang, X.; Liu, W. S.; Lu, X.; Lee, P. S. Dodecyl Sulfate-induced Fast Faradic Process in Nickel Cobalt Oxide-Reduced Graphite Oxide Composite Material and its Application for Asymmetric Supercapacitor Device. *J. Mater. Chem.*, **2012**, *22*, 23114-23119

[65] Ding, R.; Qi, L.; Jia, M.; Wang, H.; Facile and Large-scale Chemical Synthesis of Highly Porous Secondary Submicron/micron-sized $NiCo_2O_4$ Materials for High-performance Aqueous Hybrid AC-$NiCo_2O_4$ Electrochemical Capacitors. *Electrochim. Acta*, **2013**, *107*, 494-502

[66] Xu, K.; Li, W.; Liu, Q.; Li, B.; Liu, X.; An, L.; Chen, Z.; Zou, R.; Hu, J. Hierarchical Mesoporous $NiCo_2O_4$@MnO_2 Core-Shell Nanowire Arrays on Nickel Foam for Aqueous Asymmetric Supercapacitors. *J. Mater. Chem. A*, **2014**, *2*, 4795-4802

[67] Tamboli, M. S.; Dubal, D. P.; Patil, S. S.; Shaikh, A. F.; Deonikar, V. G.; Kulkarni, M. V.; Maldar, N. N.; Inamuddin, Asiri, A. M.; Gomez-Romero, P.; Kale, B. B.; Patil, D. R.; Mimics of microstructures of Ni substituted $Mn_{1-x}Ni_xCo_2O_4$ for high energy density asymmetric capacitors. *Chem. Eng. J.*, **2017**, 307, 300-310

Figure captions

Fig. 1 (a) XRD profiles of $RuCo_2O_4$ thin film deposited on the SS electrode at various scan rates RCO25, RCO50 and RCO100. High magnified XPS spectra of (b) Ru3d and C1s (c) Co2p, (d) O 1s for $RuCo_2O_4$ mesoporous nanoflakes (RCO100).

Fig. 2 FE-SEM pictures of $RuCo_2O_4$ thin films prepared at different scan rates such as (a, b) RCO25 (25 mV/s), (c, d) RCO50 (50 mV/s) and (e, f) RCO100 (100 mV/s) at two different magnifications, respectively. In addition, (g-j) SEM and corresponding EDS mapping images for RCO100 sample.

Fig. 3 TEM and HRTEM analysis of the RuCo2O4 mesoporous nanoflakes (RCO100 sample): (a) Low-magnified TEM, (B) high magnified image presenting mesoporous feature (c) STEM image further confirming homogeneous distribution of nano-particles, (d) HRTEM image with corresponding lattice fringes and (e) SAED pattern.

Fig. 4 (a) The nitrogen adsorption/desorption isotherms with (b) corresponding pore size distribution curve for RCO100 sample.

Fig. 5 (a) The CV profiles for all $RuCo_2O_4$ electrodes at 40 mV/s scan rate of in 2 M KOH electrolyte. (b) CV profiles for RCO100 sample at various scan rates from 5-100 mV/s and (c) The plot of anodic and cathodic current with respect to scan rate

Fig. 6 (a) charge-discharge curves for $RuCo_2O_4$ electrodes at 6.6 A/g in 2 M KOH electrolyte. (b) charge-discharge curves for the RCO100 sample at current densities of 6.6, 13, 20, 26, 33, 40 A/g (c) the comparison of specific and areal capacitances for RCO25, RCO50 and RCO100 samples and (d) plot of specific capacitance with current density for RCO25, RCO50 and RCO100 samples.

Fig. 7 (a) Nyquist plot of $RuCo_2O_4$ electrodes with enlarged view in the inset within a frequency range of 0.1 Hz to 105 Hz (b) plot of log f vs. phase angle (θ) (c) log f vs. log|Z| and (d) real and imaginary capacitances (C' and C") vs. frequency (log f) of $RuCo_2O_4$ thin films in 2 M KOH electrolyte.

Fig. 8 cycling performance of the $RuCo_2O_4$ electrode (RCO100) by GCD at gradual increasing current densities. Inset figures shows the first and last three GCD cycles

Fig. 9 (a) CV profiles for $RuCo_2O_4$//AC asymmetric supercapacitor at scan rate of 5 -100 mV/s within potential limit of 1.4 V, (b) the charge-discharge curves for $RuCo_2O_4$//AC asymmetric supercapacitor at various current densities, (c) representative charge-discharge curves at current density of 1.2 A/g for $RuCo_2O_4$//AC asymmetric supercapacitor and (d) the variation of the specific and volumetric capacitance with current density for $RuCo_2O_4$//AC asymmetric supercapacitor

Fig. 10 (a) Ragone plot for $RuCo_2O_4$//AC asymmetric supercapacitor device and (b) the plot of Coulombic efficiency and capacitance retention with cycle numbers.

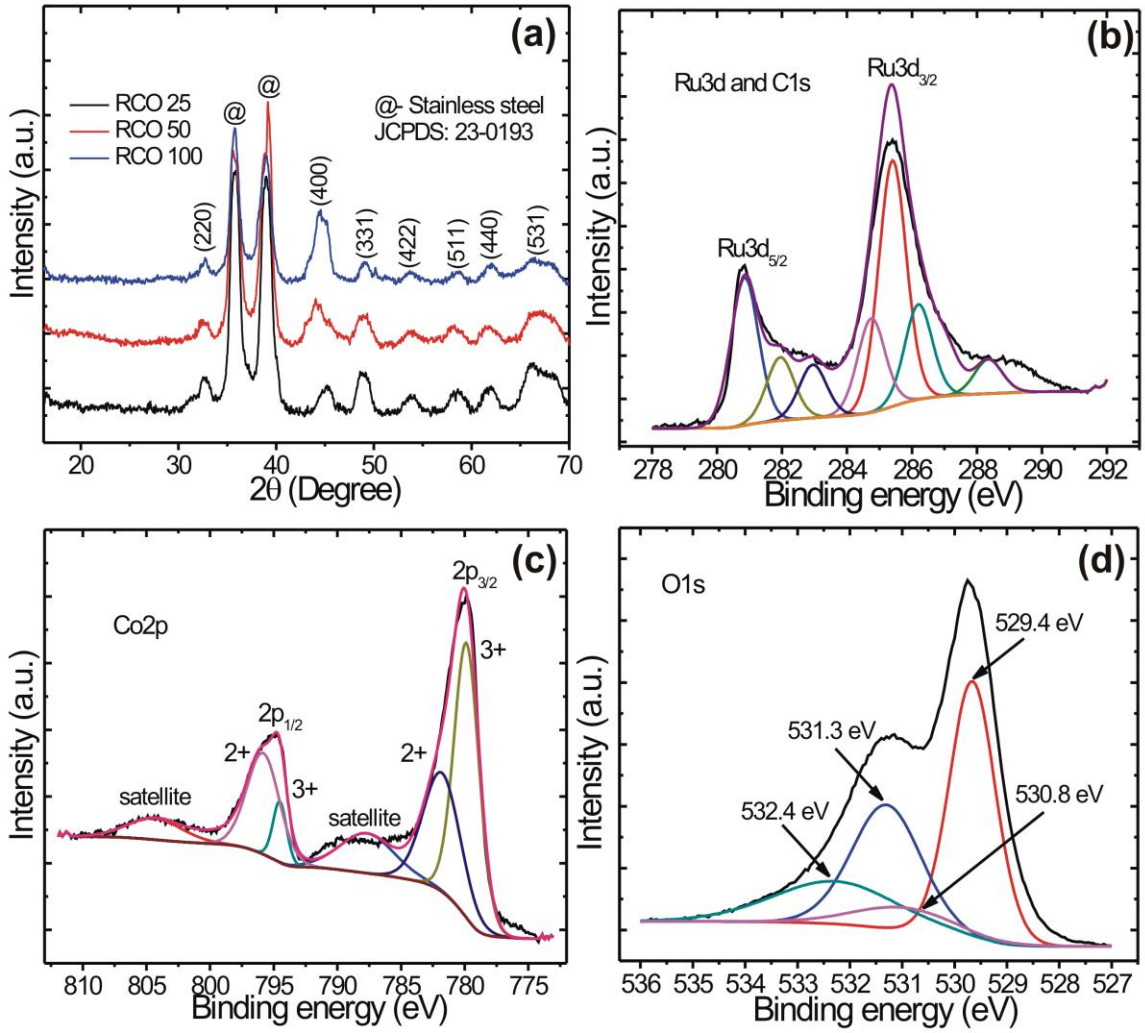
(a)
RCO 25
RCO 50
RCO 100
@- Stainless steel
JCPDS: 23-0193
@
@
(220)
(400)
(331)
(422)
(511)
(440)
(531)
Intensity (a.u.)
2θ (Degree)
(b)
Ru3d and C1s
Ru3d3/2
Ru3d5/2
Intensity (a.u.)
Binding energy (eV)
(c)
Co2p
2p3/2
3+
2p1/2
2+
2+
3+
satellite
satellite
Intensity (a.u.)
Binding energy (eV)
(d)
O1s
529.4 eV
531.3 eV
532.4 eV
530.8 eV
Intensity (a.u.)
Binding energy (eV)

Fig. 1

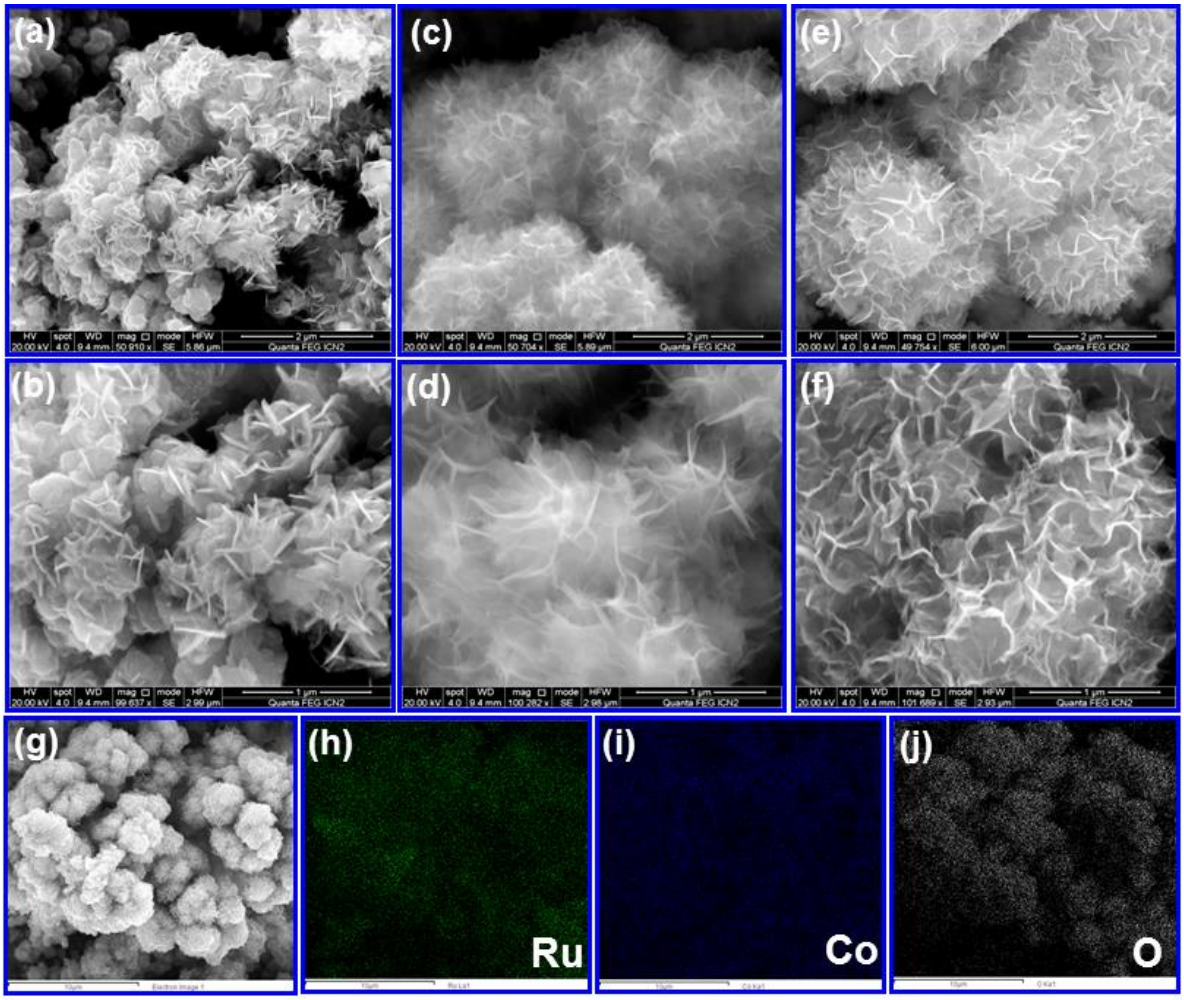

Fig. 2

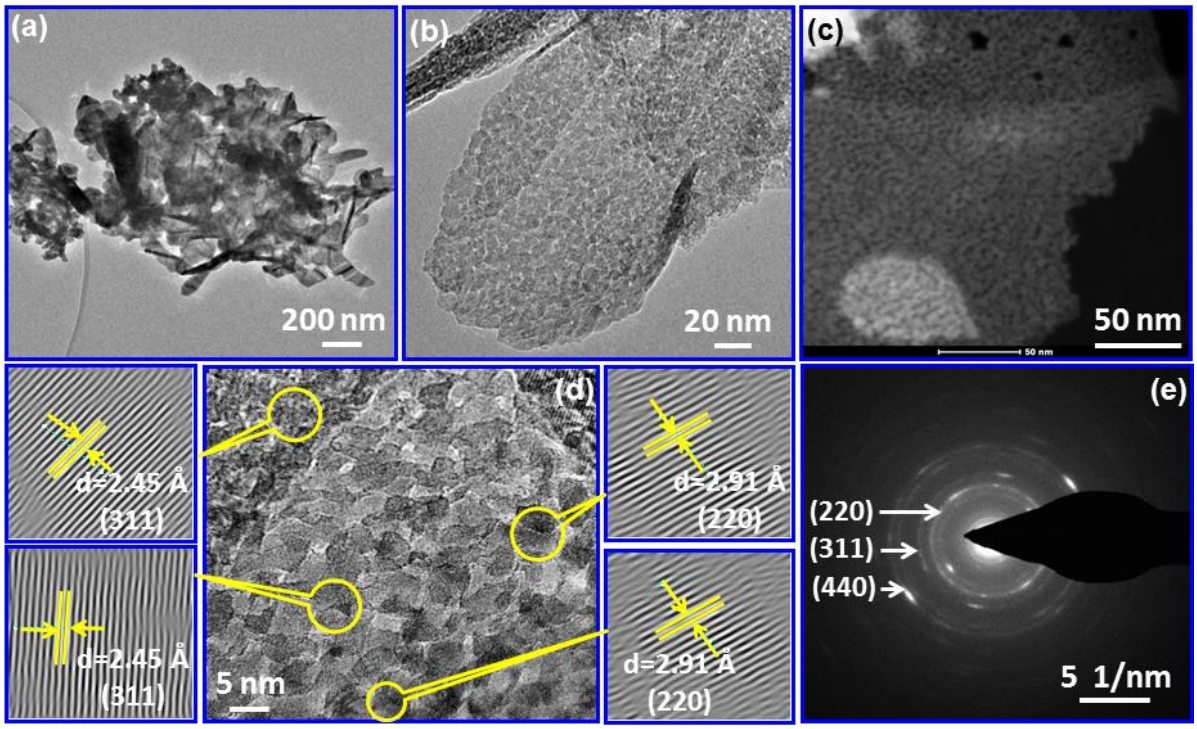
(a)
200 nm
(b)
20 nm
(c)
50 nm
d=2.45 Å
(311)
(d)
d=2.91 Å
(220)
d=2.45 Å
(311)
5 nm
d=2.91 Å
(220)
(e)
(220)
(311)
(440)
5 1/nm

Fig. 3

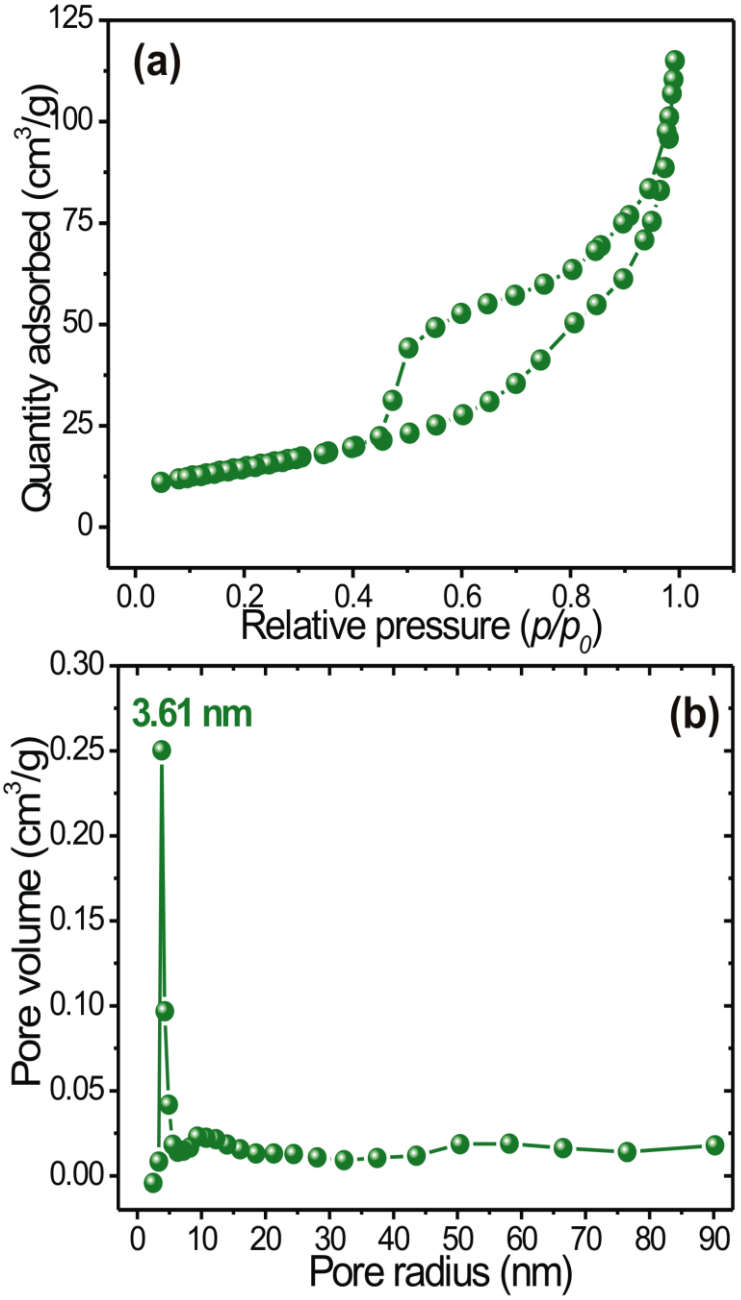
(a)
Quantity adsorbed (cm³/g)
Relative pressure (p/p0)
(b)
3.61 nm
Pore volume (cm³/g)
Pore radius (nm)

Fig. 4

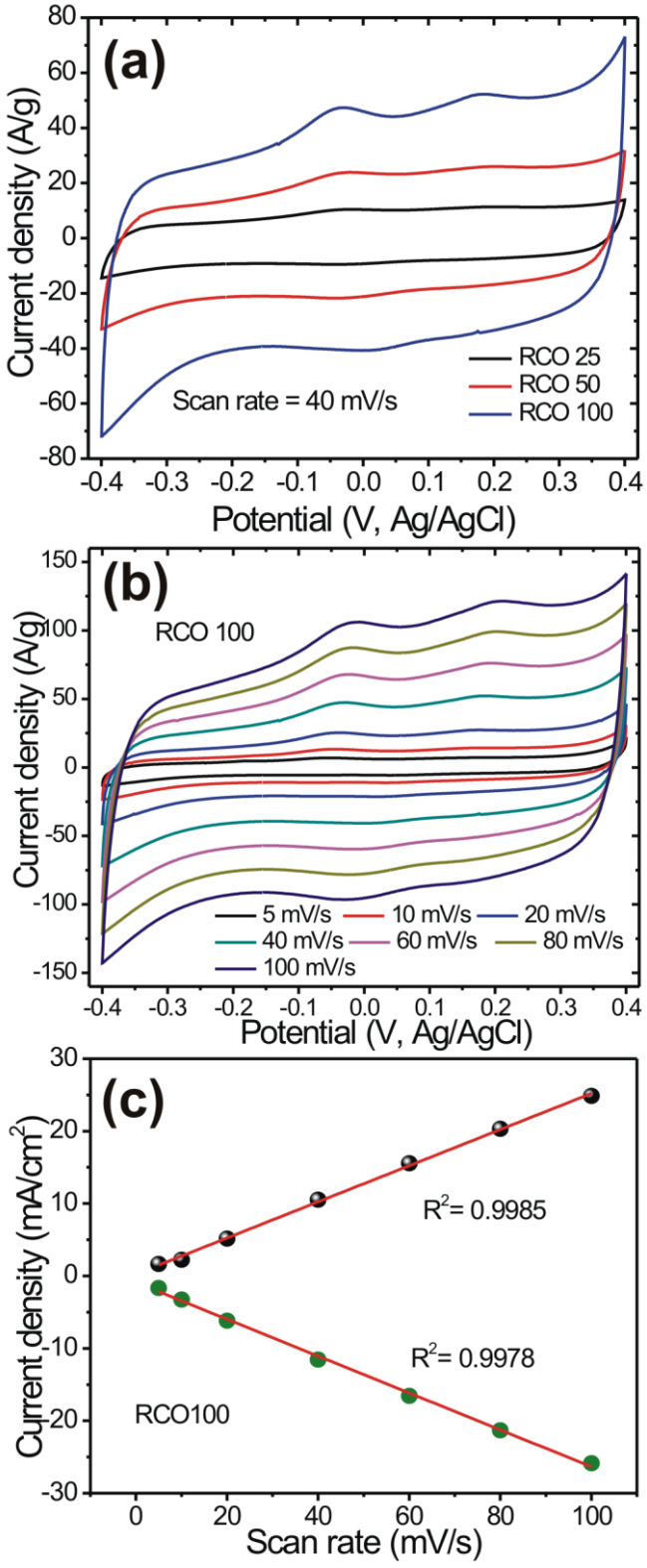
(a)
Current density (A/g)
Potential (V, Ag/AgCl)
Scan rate = 40 mV/s
RCO 25
RCO 50
RCO 100
(b)
RCO 100
Current density (A/g)
Potential (V, Ag/AgCl)
5 mV/s
10 mV/s
20 mV/s
40 mV/s
60 mV/s
80 mV/s
100 mV/s
(c)
Current density (mA/cm2)
Scan rate (mV/s)
R2= 0.9985
R2= 0.9978
RCO100

Fig. 5

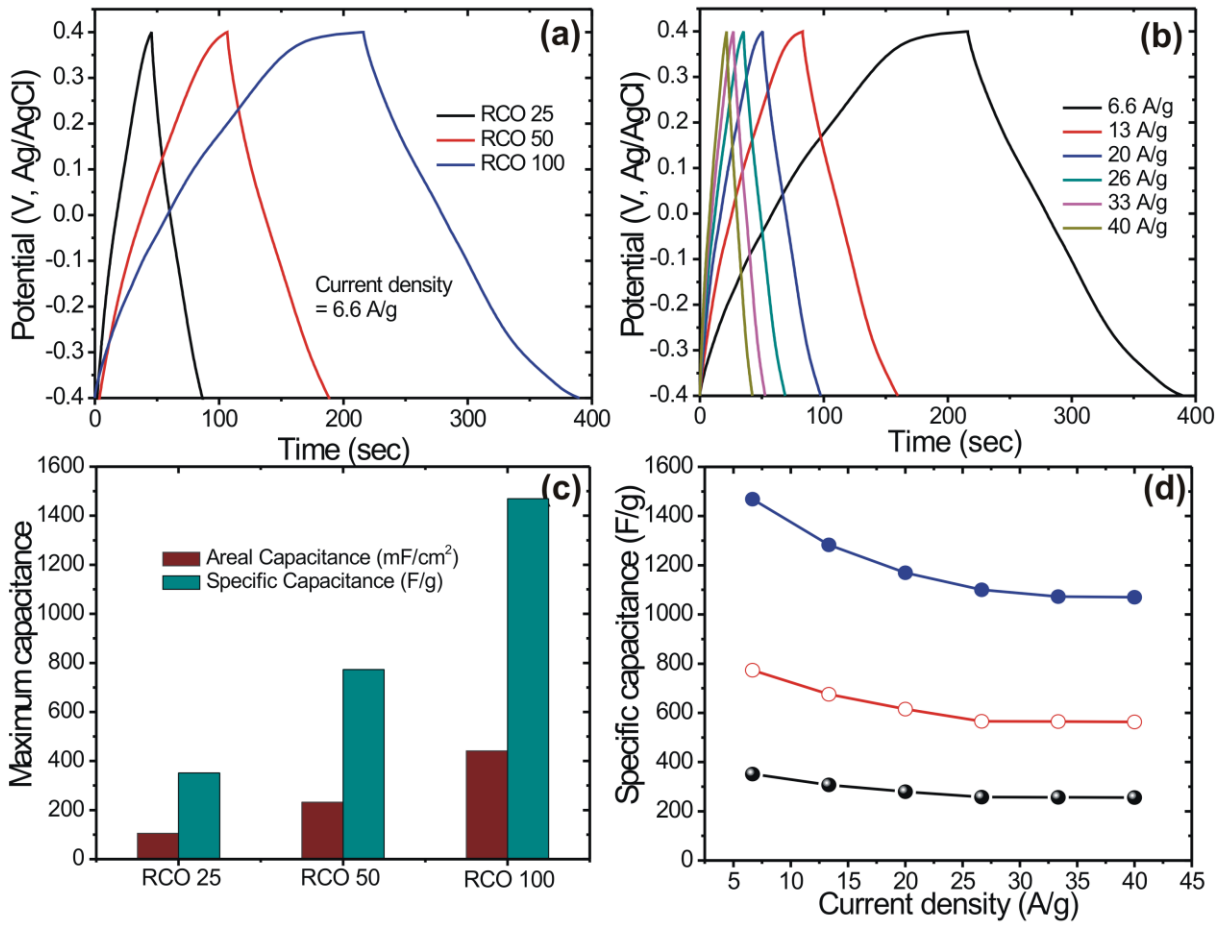
(a)
Potential (V, Ag/AgCl)
Time (sec)
RCO 25
RCO 50
RCO 100
Current density
= 6.6 A/g
(b)
Potential (V, Ag/AgCl)
Time (sec)
6.6 A/g
13 A/g
20 A/g
26 A/g
33 A/g
40 A/g
(c)
Maximum capacitance
Areal Capacitance (mF/cm^2)
Specific Capacitance (F/g)
RCO 25
RCO 50
RCO 100
(d)
Specific capacitance (F/g)
Current density (A/g)

Fig. 6

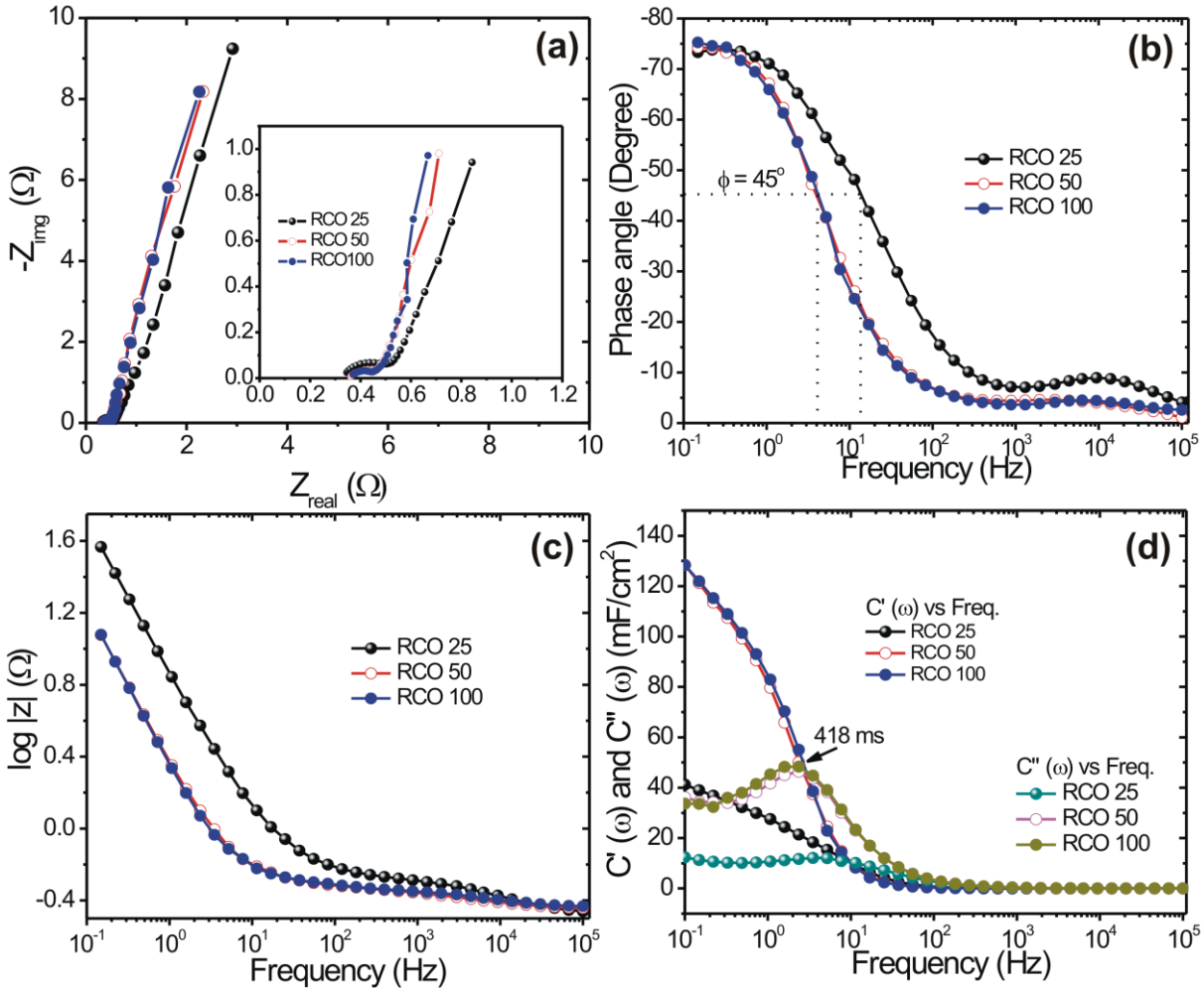
(a)
-Z_img (Ω)
Z_real (Ω)
RCO 25
RCO 50
RCO100
(b)
Phase angle (Degree)
ϕ = 45°
RCO 25
RCO 50
RCO 100
Frequency (Hz)
(c)
log |z| (Ω)
RCO 25
RCO 50
RCO 100
Frequency (Hz)
(d)
C' (ω) and C'' (ω) (mF/cm²)
C' (ω) vs Freq.
RCO 25
RCO 50
RCO 100
418 ms
C'' (ω) vs Freq.
RCO 25
RCO 50
RCO 100
Frequency (Hz)

Fig. 7

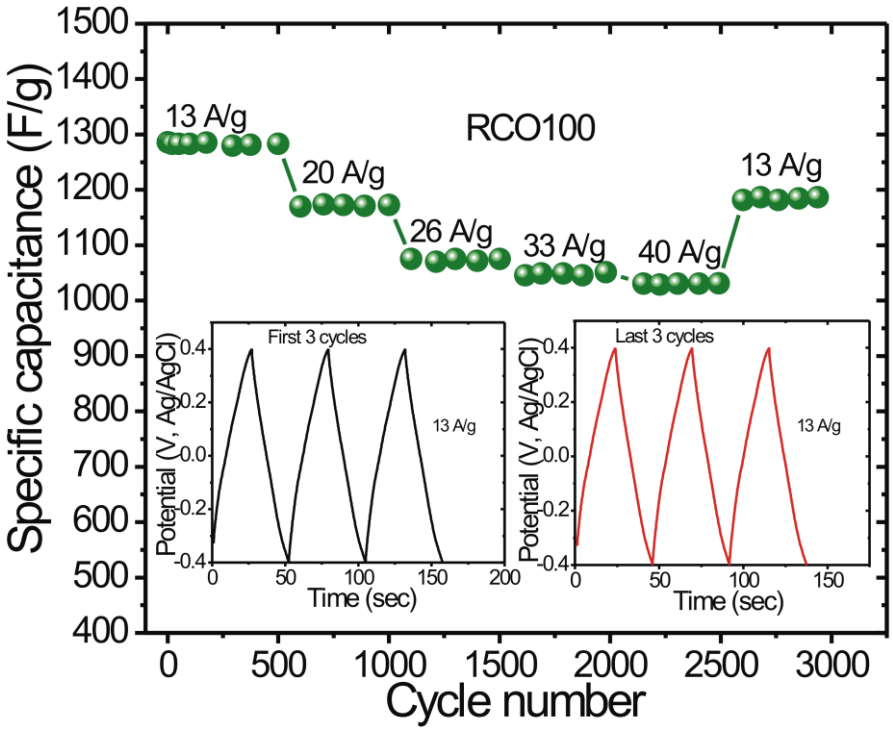
Specific capacitance (F/g)
Cycle number
RCO100
13 A/g
20 A/g
26 A/g
33 A/g
40 A/g
13 A/g
First 3 cycles
Last 3 cycles
Potential (V, Ag/AgCl)
Time (sec)
13 A/g

Fig. 8

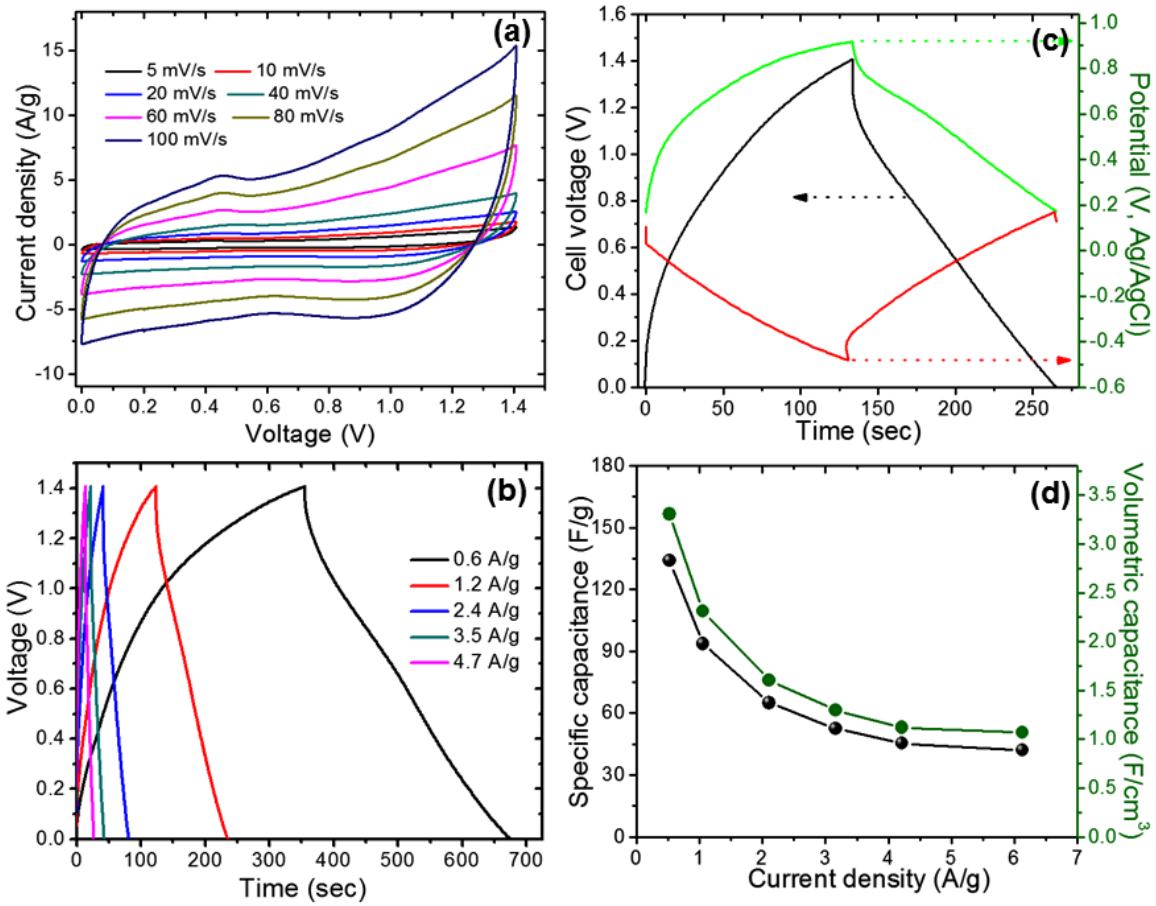
(a)
5 mV/s
10 mV/s
20 mV/s
40 mV/s
60 mV/s
80 mV/s
100 mV/s
Current density (A/g)
Voltage (V)
(c)
Cell voltage (V)
Potential (V, Ag/AgCl)
Time (sec)
(b)
0.6 A/g
1.2 A/g
2.4 A/g
3.5 A/g
4.7 A/g
Voltage (V)
Time (sec)
(d)
Specific capacitance (F/g)
Volumetric capacitance (F/cm3)
Current density (A/g)

Fig. 9

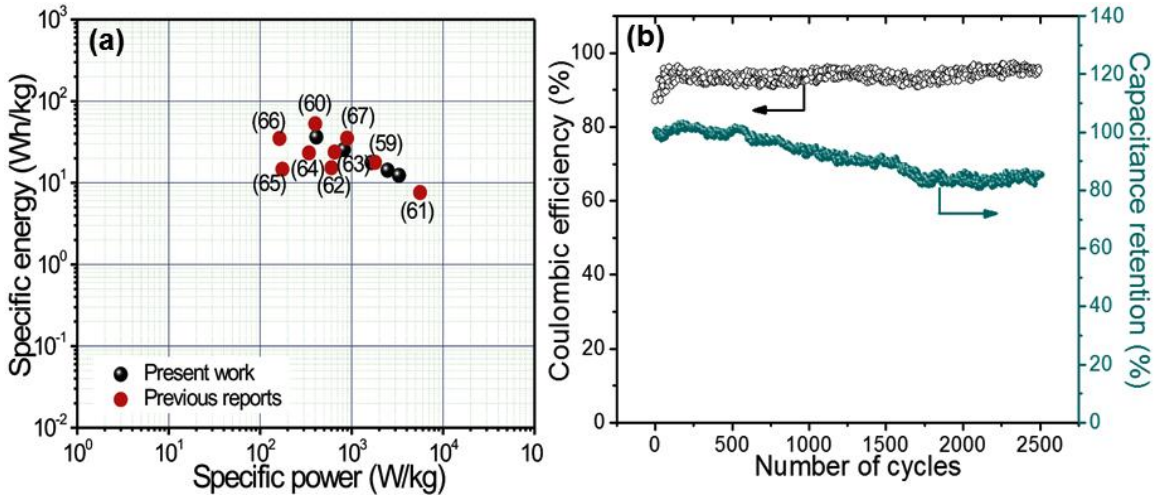
(a)
Specific energy (Wh/kg)
Specific power (W/kg)
Present work
Previous reports
(60)
(66)
(67)
(59)
(64)
(63)
(65)
(62)
(61)
(b)
Coulombic efficiency (%)
Capacitance retention (%)
Number of cycles

Fig. 10